

# Vertical ocean heat fluxes beneath Linear Kinematic Features in the Arctic Ocean

Alexander Slavin,<sup>1</sup> Bruno Tremblay,<sup>1</sup> David Straub<sup>1</sup>

---

Corresponding author: Alexander Slavin, McGill University, Department of Atmospheric and Oceanic Sciences, Montreal, Quebec, Canada. (alexander.slavin@mcgill.ca)

<sup>1</sup>McGill University, Department of  
Atmospheric and Oceanic Sciences,  
Montreal, Quebec, Canada.

**Abstract.** Measured ocean heat fluxes in the central Arctic are typically small in winter - of the order of  $1 \text{ W/m}^2$  or smaller. In fact the Cold Halocline Layer (CHL) - a layer of cold but saltier waters beneath the mixed layer and above the Atlantic waters - provide a strong barrier to vertical exchange in the surface ocean. In this paper, we show modeling evidence, supported by observations, for strong Ekman pumping velocities beneath active leads (Linear Kinematic Features, LFKs) where discontinuity in the sea-ice drifts and the surface ice-ocean stresses momentum transfer are present. To this end, we use a high resolution ( $3.75 - 5.5 \text{ km}$ ) coupled ice-ocean model with a good representation of the CHL and Near Surface Temperature Maximum (NTSM) - the MITgcm - forced with contemporaneous atmospheric forcing from the Japanese Reanalysis Project (JRA-25). Simulated vertical velocities near LKFs can extend hundreds of meters below the surface, into the Warm Atlantic Layer. Typical vertical displacements in an LKF event, however, are only a few tens of meters. As such, we argue that anomalous heat fluxes under LKFs bring up heat from the shallower NSTM, and possibly the Summer Pacific Waters. To assess the overall impact of LKF-related heat fluxes on the sea ice mass balance, we apply a simple linear relationship between the observed ocean heat flux beneath an active LKF (McPhee et al., 2005), sea-ice velocity curl from the Radarsat Geophysical Processor System (RGPS) and Polar Pathfinder sea ice velocities. We focus on the Beaufort Sea, a region of intense active LKFs. Averaged over the Beaufort Sea, results suggest that wintertime heat fluxes associated with Ekman pumping beneath

active LKFs are sufficient to melt about 11 cm of sea ice ( $1 \text{ W/m}^2$ ). We suggest that this process can be important in controlling the Arctic sea-ice mass balance and a potentially important player in the recent sea-ice decline in the Beaufort Sea one that is not represented in lower-resolution global climate models. Additionally, projections of a thinning and more mobile pack ice suggest that LKF-related heat fluxes will amplify under near-future climate scenarios.

## 1. Introduction

In the last decades, the Arctic has experienced the largest and most rapid warming in the Northern Hemisphere [*Hansen et al.*, 2006; *Comiso*, 2006]. The minimum in Arctic sea-ice extent at the end of the summer melt season has declined at a rate of approximately 7.8% per decade over the period between 1953 - 2006 [*Stroeve et al.*, 2007], with this value increasing to 12.2% per decade over the period of modern satellite observations [*Comiso*, 2012]. In 2012 the minimum sea-ice extent was approximately half (3.41 million km<sup>2</sup>) of the 1979-2000 average (6.7 million km<sup>2</sup>) [<http://nsidc.org/arcticseaicenews/2012/09/arctic-sea-ice-extent-settles-at-record-seasonal-minimum>]. Increased open water formation leads to an increase in solar radiation absorbed in the surface ocean and this in turn accelerates the ice retreat (sea ice albedo feedback). Several global climate models participating in the Coupled Model Intercomparison Project - Phase 5 (CMIP5) still underestimate the observed sea ice decline [*Stroeve et al.*, 2012]. GCMs simulating the most aggressive sea-ice decline suggest that the Arctic could become ice-free at the end of the summer as early as 2040, [e.g. *Holland et al.*, 2006]. Large simulated inter-decadal variability by GCMs however impose an uncertainty of approximately 20 years on the exact timing of an ice-free Arctic [*Kay et al.*, 2011].

Below the ocean mixed layer at around 80-200 m lies a layer of cold, low salinity water called the Cold Halocline Layer (CHL), [*Aagaard et al.*, 1981; *Rudels et al.*, 1996]. The CHL waters are formed in part on the Eurasian shelf when relatively fresh shelf water salinifies due to sea-ice formation [*Aagaard et al.*, 1981]. This water then spills over the

continental shelf and finds its level of equilibrium beneath the fresher surface waters and the relatively saltier Atlantic waters. Additional CHL waters are formed in the open ocean by brine rejection during ice formation, [Rudels *et al.*, 1996]. Below the CHL, between about 80-250 m, lies a warmer, more saline layer of Atlantic origin water, [Aagaard *et al.*, 1981]. Atlantic waters enters from the North Atlantic (West Spitsbergen Current and Barents Sea branches) and spread beneath the cold halocline. The overlying CHL, however, is thought to provide an efficient buffer, insulating the surface ocean from this large reservoir of heat.

Seasonal changes in upper ocean heat content are mainly associated with surface heat fluxes; heat exchanges with the Atlantic and Pacific play a relatively minor role, except near the ice edge [Bitz *et al.*, 2005] and where the cold halocline layer is absent, e.g., north of Svalbard, [McPhee *et al.*, 2003]. The first estimate of the ocean-to-ice heat flux comes from Maykut and Untersteiner [1971]. They used a numerical model forced with observed atmospheric fields to show that an annual mean ocean heat flux of about 2 W/m<sup>2</sup> was necessary to reproduce the observed seasonal cycle in ice thickness. Later Maykut and Perovich [1987] and Maykut and McPhee [1995] showed that the source for this ocean-to-ice heat flux was summertime downwelling shortwave radiation entering the ocean mixed layer through leads and thinner ice. This was based on the observed surface shortwave radiation, CTD measurements, and open water area estimates derived from the deformation of the AIDJEX experiment manned triangle. This implies a strong seasonality in ocean heat fluxes, with values of 40-60 W/m<sup>2</sup> in summer. Absorption of solar heat in summer translates efficiently into sea ice loss, especially in recent years when more open water and thinner ice has been present in large portion of the Arctic. For

instance during the SHEBA field campaign, 49% of the summer total melt occurred at the ice base [Perovich *et al.*, 2003]. In fall, however, this heat is partially ventilated and by winter, vertical ocean heat fluxes typically drop to much smaller levels, e.g., 1-2 W/m<sup>2</sup> or smaller.

## Problématique!

Recently, Rudels *et al.* [2004] pointed out that the heat contained in the Atlantic layer is sufficient to completely melt the Arctic sea-ice cover, provided it could be transported up to the surface. In the last decades, a significant warming of the Atlantic layer was observed, with maximum temperatures more than 1°C warmer in the 1990s as compared to period between 1950 and 1989, [Morison *et al.*, 2000; Serreze *et al.*, 2000; Shimada *et al.*, 2004]. This warming continued to accelerate in 2000s [Schauer *et al.*, 2004; McLaughlin *et al.*, 2009; Polyakov *et al.*, 2011; Lind and Ingvaldsen, 2012]. It is widely considered, however, that the cold halocline almost completely protects the ice cover from this heat source. In fact, recent measurements from ice-tethered profiler show only a very small ocean heat flux of Atlantic origin by double staircase diffusion [Timmermans *et al.*, 2008]. Other estimates have also pointed to low values. Rudels *et al.* [1996] estimate 1.3 W/m<sup>2</sup> for the eastern Laptev Sea using double-diffusion convection heat flux calculation; Steele and Boyd [1998] obtained 1-3 W/m<sup>2</sup> in the Eurasian Basin using a simple mixed-layer ocean model; a winter mean ocean heat flux of 2 W/m<sup>2</sup> was measured during the Surface Heat Budget of the Arctic Ocean (SHEBA) experiment [Perovich and Elder, 2002]. Using a parameterization based on satellite-derived daily ice drifts and an in situ data set, Krishfield and Perovich [2005] report an increase of up to 3-4 W/m<sup>2</sup> throughout the Arctic Ocean icepack. This ocean heat flux is thought to originate from solar radiation entering the mixed layer through leads, rather than, say, from vertical advection or diffusion. Using

a combination of 1D and 3D GCM modeling, *Polyakov et al.* [2010] have shown evidence of ocean warming at depth, as well as a small increase (of about  $0.5 \text{ W/m}^2$ ) in ocean heat flux. Citing model limitations, however, they place limited confidence in this simulated increase. Another possibility, suggested by [Morison, 1980], is that heat is brought to the surface in association with convection fueled by brine rejection when ice forms in newly opened leads (or LKFs).

While winter measurements of vertical ocean heat fluxes reported in the literature are typically small, there are a few exceptions where larger values have been observed along the continental shelf break. For example, *McPhee et al.* [2003] measured an average value around  $22 \text{ W/m}^2$  over the Yermak Plateau, a region where the CHL is absent and strong tidal mixing is present. Additionally, during the SHEBA experiment, the ice camp drifted over the Northwind Ridge in March [Huwald et al., 2005; Perovich and Elder, 2002; Shaw et al., 2009], and the ocean heat flux increased to approximately  $20 \text{ W/m}^2$ . *Yang et al.* [2004] showed that large ocean heat fluxes are present associated with Ekman-driven upwelling during intense storms along the continental shelf (where the CHL is absent). Of particular interest for the present study are measurements made during the SHEBA experiment taken in the vicinity of an active lead; where surface heat fluxes as large as  $380 \text{ W/m}^2$  at 9.9 m depth were found, [McPhee et al., 2005]. The authors hypothesize that Ekman pumping associated with a positive ice-ocean surface stress curl brought heat from beneath the mixed layer into the mixed layer. The origin of this heat is believed to be relic heat of atmospheric origin from a previous summer trapped beneath the mixed layer (*M. McPhee*, personal communications). Recently *Lei et al.* [2014] investigated oceanic heat fluxes utilizing an ice mass balance buoy. From mid-November 2008 to mid-

June 2009, they measured an average oceanic heat fluxes of  $7.1 \text{ W/m}^2$  along a track from  $86.2^\circ\text{N}$ ,  $115.2^\circ\text{W}$  to  $84.6^\circ\text{N}$ ,  $33.9^\circ\text{W}$ . This relatively large oceanic heat flux was attributed to the heat deposited in the upper ocean during the preceding summer and early autumn.

In this paper we investigate whether discontinuities in the ice-ocean momentum transfer across linear kinematic features (LKFs) in the sea-ice cover can lead to significant vertical advection, providing a pathway whereby heat from the Near Surface Temperature Maximum [Jones *et al.*, 1998] or the warmer Pacific/Atlantic water can be ventilated in the surface mixed layer, thereby affecting the winter sea-ice mass balance. Ice velocities are discontinuous across shear lines; consequently, so are the ice-ocean momentum transfer and the Ekman transport below the ice. One therefore expects to see strong vertical velocities in the upper ocean associated with LKFs.

To this end, we use a high resolution coupled ice-ocean model (the MITgcm, with horizontal resolution ranging from 3.75 to 5.5 km) to assess whether the Ekman pumping velocity associated with discontinuities in the ice-ocean surface stress are ubiquitous features of the Arctic sea ice cover and, if so, whether this results in a significant amount of heat being carried up from depth to the surface. We find that, LKFs can lead to a significant vertical heat transport. Additionally, although vertical velocities associated with LKF-Ekman pumping do extend into the Atlantic layer, vertical displacements are smaller, so that heat reaching the surface likely comes from a shallow source; for example, relic heat trapped beneath the mixed layer from previous summers or summer Pacific Waters beneath the CHL.



The paper is organized as follows. In Section 2, the numerical model and numerical experiments are presented. In Section 3, results from the model and their discussions are presented. The main conclusions of the paper are summarized in Section 4.

## 2. Numerical Model

We use the regional coupled ice–ocean model version of the Massachusetts Institute of Technology general circulation model (MITgcm) [Marshall *et al.*, 1997a, b] for direct numerical simulations of the Arctic Ocean. This version of the model is publicly available from the consortium for Estimating the Circulation and Climate of the Ocean (ECCO–Jet Propulsion Laboratory ecco.jpl.nasa.gov).

The model is configured on a cube sphere. Our domain uses the cube face having boundaries at  $55^{\circ}N$ . As such, it includes the entire Arctic, as well as parts of the North Atlantic and North Pacific oceans. The model uses 50 vertical levels and a locally orthogonal curvilinear grid. Horizontal resolution varies between 3.75 km and 5.5 km (see Figure 1) and vertical grid spacing ranges between 10 m in the upper 100 m to 456.5 m at the bottom. The model is integrated using a finite volume discretization. We use the non-linear equation of state formulated by Jackett and McDougall [1995], the K-Profile Parameterization (KPP) vertical mixing scheme of Large *et al.* [1994], a biharmonic Leith viscosity in the momentum equation, and a 7<sup>th</sup> order direct space time with flux limiter advection scheme for temperature and salinity [Daru and Tenaud, 2004].

The MITgcm sea-ice model is based on a viscous-plastic rheology with elliptical yield curve and normal flow rule [Hibler, 1979]. The momentum equations are solved on a C-grid [Arakawa and Lamb, 1977] using an Alternating Direction Implicit numerical scheme developed by Zhang and Hibler [1997]. A two-category (mean ice thickness and con-

centration) sea ice thermodynamic model predicts the mean ice thickness and sea ice concentration (fraction of a grid cell that is covered by sea ice). Salt rejected during sea-ice formation is treated using a subgrid scale salt plume parameterization developed by *Menemenlis et al.* [2005] and *Nguyen et al.* [2009]. This parameterization allows for a realistic halocline vertical profiles [*Menemenlis et al.*, 2005; *Nguyen et al.*, 2009] and reduces model bias and drift.

The ice-ocean turbulent heat flux is parametrized as a function of the temperature difference between the mixed layer and freezing point temperature of sea water. This flux is used to melt ice or freeze ocean water, and relax the mixed layer temperature to its freezing point, with a relaxation time scale of three days. Lateral and vertical growth of sea ice is parametrized using a fixed demarcation for the thickness of newly formed sea ice [*Hibler*, 1979, 1980]. False bottom ice formation, associated with downward diffusion of heat between the fresher relatively warm melt water lens beneath sea ice and the more saline relatively cold mixed layer waters [false bottom *Notz et al.*, 2003], is not included in the mitcgm.

Initial conditions for temperature and salinity come from the World Ocean Atlas (WOA05) ([www.nodc.noaa.gov/OC5/WOA05/woa05data.html](http://www.nodc.noaa.gov/OC5/WOA05/woa05data.html)). Prescribed boundary conditions for potential temperature, salinity, ocean velocity, and sea surface elevation are provided from an integration of a global configuration of the same model [*Menemenlis et al.*, 2005]. No-slip bottom, free-slip lateral, and ocean free surface boundary conditions are used in all simulations. Virtual salt fluxes are used for freshwater fluxes associated with river runoff. The model is forced with 6-hourly atmospheric fields from the Japanese 25-year Reanalysis Project (JRA-25, [jra.kishou.go.jp](http://jra.kishou.go.jp)). Monthly mean runoffs are spec-

ified from the Arctic runoff database of *Lammers et al.* [2001]. The ocean and sea ice model time step used in the simulations are both equal to 240 seconds. Numerical experiments were performed at the McGill University’s Centre for High Performance Computing (McGill HPC) ([www.hpc.mcgill.ca](http://www.hpc.mcgill.ca)). A typical numerical simulation used 320 CPU cores. The main parameters of numerical simulations are summarized in Table 1.

### 3. Results

#### 3.1. Spin-up

The model was first spun up for 20 years to approximate cyclostationarity using a random permutation of forcing years to avoid biases associated with a given phase of the Arctic Oscillation. Starting from the end of this 20 year integration, 10 one-year simulations were next carried out. For these, forcing fields corresponding to individual years between 1991 and 2000 were used. We first consider the ensemble average of these one year simulations.

To assess possible errors relating to model drift, we examine the seasonal cycle of the fresh water content in the upper 10, 100 and 207 meters (see Figure 2). Fresh water content provides a stringent test for cyclostationarity and is thus a good proxy for model drift; for instance, 3 models out of the 6 models participating in the Arctic ocean intercomparison project require restoring on salinity to keep the model stable, whereas only 1 model require restoring on both salinity and temperature [*Uotila et al.*, 2006]. The linear trends in fresh water content ( $-0.0003$ ,  $0.0003$  and  $0.0007$ ) over the three depths considered are not statistically different from zero with significance at the 95% level. We take this as evidence that model drift is sufficiently weak.

### 3.2. Surface ocean heat budget

We next consider a monthly-averaged energy balance equation for the Arctic Ocean surface layer (see Figure 3). The internal energy,  $E$ , evolves according to:

$$\begin{aligned} \frac{dE}{dt} &= \frac{\rho_w C_{pw}}{\Delta t} \int_{-H}^0 (T_{of}(z) - T_{oi}(z)) dz = \\ &= F_{sw} + F_{lw} + F_{SH} + F_{LH} + F_{io} + F_{fraz} + F_{v-diff} + F_{v-adv}. \end{aligned} \quad (1)$$

Here,  $H = 40$  m is the approximate winter mixed-layer thickness, and  $T_{of}$  and  $T_{oi}$  are the final and initial ocean temperature for a given month. The net shortwave and longwave radiation entering the ocean surface layer are given by  $F_{sw}$  [ $= F_{sw\downarrow}(1 - \alpha_o)(1 - A)$ ] and  $F_{lw}$  [ $= F_{lw\downarrow}\epsilon_o + \epsilon_o\sigma T_{surf}^4(1 - A)$ ], respectively. In these expressions,  $A$  is the sea-ice concentration,  $F_{sw\downarrow}$  and  $F_{lw\downarrow}$  are the downwelling shortwave and longwave radiation (output diagnostic from the model),  $T_{surf}$  is the surface ocean temperature. Sensible ( $F_{sen}$ ) and latent heat ( $F_{lat}$ ) fluxes into the surface waters are  $F_{SH}$  [ $= F_{sen}(1 - A)$ ] and  $F_{LH}$  [ $= F_{lat}(1 - A)$ ] are obtained from the model diagnostics. The ice-ocean turbulent heat flux,  $F_{io}$ , is largely responsible for ice melt and is also obtained as a standard output diagnostic.  $F_{fraz}$  is the latent heat flux responsible for frazil ice formation (output diagnostic from the model),  $F_{v-diff}$  is the vertical diffusive heat flux (output diagnostic from the model),  $F_{v-adv}$  [ $= W(40m)(T_w - T_{fr})$ ] is the vertical advective heat flux,  $W(40$  m) is the vertical velocity at depth  $z = 40$  m and  $T_w$  is the temperature of a grid centered at 45 m depth. Lateral ocean heat transport plays a relatively small role in the ocean surface budget [Serreze et al., 2007], and is not included. Other symbols in the equation above are defined in Table 1.

The ensemble averaged seasonal cycle for the surface heat budget is shown in Figure 3. Fluxes are defined such that positive values correspond to increases in ocean energy. In winter, vertical heat fluxes are typically small (less than  $5 \text{ W/m}^2$ ); ocean heat fluxes at the base of the mixed layer are ventilated at the surface via sensible, latent and longwave radiative fluxes. Note that some of the heat ventilated is provided by a decrease of the internal energy of the salinifying surface waters. In early and mid-summer, the fluxes are larger (tens of  $\text{W/m}^2$ ) and the main balance is between the shortwave radiative flux and the turbulent ice-ocean heat leading to sea-ice melt. Advective ocean heat fluxes, changes in internal energy of the mixed-layer and net longwave radiation are smaller and about 20% of the shortwave flux in magnitude. In late summer and early fall, shortwave radiative and turbulent ice-ocean heat fluxes reduce, sensible and latent heat fluxes increase and all fluxes are of the same order of magnitude ( $\sim 5 \text{ W/m}^2$ ).

The ensemble mean advective and diffusive vertical heat fluxes for our 10 one-year simulations are about  $3 - 4 \text{ W/m}^2$  and  $0.05 - 0.1 \text{ W/m}^2$ , respectively (Figure 3). The yearly mean residual heat flux (equal to lateral advection and diffusion of heat at the boundaries of the domain, see Figure 1) is approximately  $-0.7 \text{ W/m}^2$  – in agreement with *Serreze et al.* [2007]. In the following, we focus on the winter energy balance and in particular on the vertical advective ocean heat flux from the deeper ocean into the surface layer, the mechanism that brings this heat to the surface and the source of the heat.

### 3.3. Vertical ocean heat fluxes at the base of the mixed layer

The winter (JFM) and summer (JJA) averaged vertical diffusive and advective heat fluxes at 40, 100 and 207 m depth are shown in Figure 4 and 5, respectively. The former is a standard diagnostic output of the model and the latter is calculated relative to the

freezing point, i.e, as  $W(T_w - T_{fr})$ . At 40 m in both winter and summer (see Figure 4a-b), the diffusive heat flux is large (up to 5 W/m<sup>2</sup>) in the Barents and Chukchi Seas, where bottom friction leads to turbulence that mixes warm Atlantic or Pacific waters with colder surface Arctic water. Similarly large values are seen along much of the shelf break bordering the Nansen, Amundsen, and Canadian Basins. In the winter, large diffusive heat fluxes are also present in the interior of the Basin; these are related to eddies transporting heat laterally from the boundary current, and a subsequent vertical mixing. In the summer, stratification is higher and the diffusive heat flux is much smaller. Negative values (corresponding to a downward flux of heat) are found in Chukchi Sea; this is related to warmer Pacific surface waters mixing with colder water below that are leftover from the previous winter.

Deeper down and seaward of the shelf break, there is little seasonality and the diffusive fluxes are uniformly positive (see Figure 4c-d-e-f). Typical values are around 0.2 – 0.3 W/m<sup>2</sup> at 100 m and 0.05 W/m<sup>2</sup> at 207 m. At 100 m, large values are located near the boundary current on the Eurasian side of the Arctic, the Lomonosov ridge, and in the interior of the Nansen, Amundsen and Canada Basins. This is consistent with observations from [Sundfjord *et al.*, 2007; Woodgate *et al.*, 2001]. They found eddies from boundary currents to transfer heat to the basin interior at depth, with subsequent vertical mixing. At 207 m, diffusive fluxes are smaller and are concentrated on the North American side of the Canada, Amundsen and Nansen Basins, where the maximum vertical temperature gradient is found. The mean diffusive fluxes at 207 m in the open ocean (depths larger than 2000 m) is 0.012 W/m<sup>2</sup> and the flux at 40 m averaged over the continental shelf break (depths between 300 and 2000 m) is 0.5 W/m<sup>2</sup>. This is in general agreement with

observations of  $0.05 - 0.3 \text{ W/m}^2$  at 200-300 m over the open ocean [Timmermans *et al.*, 2008] and somewhat smaller than observations of  $3 - 10.7 \text{ W/m}^2$  at 10-40 m over the shelf break. This may be related to topographical features which can induce large vertical motion and increased mixing [Sundfjord *et al.*, 2007; Polyakov *et al.*, 2010].

Vertical advective fluxes are calculated relative to the freezing point and are localized mainly along topographical features such as the shelf break and major seafloor ridges as well as on the outer Eurasian continental shelf (see Figure 5). They increase with depth from about 20 to  $200 \text{ W/m}^2$  as one approaches the maximum temperature of the Atlantic Water layer (Figure 5). The mean advective vertical heat fluxes at 25 m over open ocean and continental shelf are  $1.6 \text{ W m}^2$  and  $6.5 \text{ W m}^2$ , respectively (not shown). These fluxes are of the same order of magnitude as observed values (of about  $2.6$  and  $22 \text{ W m}^{-2}$  at the same depth McPhee *et al.* [2003]; Polyakov *et al.* [2010]).

### 3.4. Ekman pumping beneath active LKFs

In order to properly simulate the magnitude of the vertical ocean heat flux in the Arctic Ocean and more particularly beneath active LKFs, a good representation of the vertical T-S structure in the ocean is necessary. The simulated surface mixed layer, Near Surface Temperature Maximum [NSTM Jones *et al.*, 1998; Jackson *et al.*, 2010], Cold Halocline Layer [CHL Rudels *et al.*, 1996] and the Atlantic layer for the Canada Basin are shown in Figure 6. Results are in good agreement with the Polar Science Center Hydrographic Climatology (PHC), World Ocean Atlas 2005 (WOA2005) and World Ocean Atlas 2009 (WOA2009). This is in part due to a new brine rejection parameterisation that feeds the cold halocline water with cold saline waters when ice forms and rejects brine [Menemenlis *et al.*, 2005; Nguyen *et al.*, 2009].

In this section, we focus on vertical ocean advective heat fluxes beneath active LKFs and at the base of the mixed-layer (depth = 40m). To this end, we analyze two cases with different combinations of positive and negative ice-ocean stress curl and sea-ice divergence. Our goal is to test the Ekman pumping hypothesis of *McPhee et al.* [2005] (See Figures 7-8). For positive ice-ocean surface stress curl, divergence in the surface Ekman transport leads to upwelling below. Assuming warmer waters below the mixed-layer, an upward vertical heat transport is implied. By contrast, negative curl implies downwelling; in this case, the vertical heat transport from the base of the mixed-layer is small, since the mixed-layer temperature is at the freezing point. The vertical ocean heat flux near leads is thus expected to be a function the ice-ocean surface stress curl and the heat contained (referenced to the freezing point) in the halocline layer (NSTM). Note that there is also another mechanism for bringing ocean heat to the surface along active LKFs. This is associated with sea-ice divergence and formation of new ice. Brine rejection then leads to convection, and this can transport heat (if present) upward from the halocline layer [Morison, 1980]. For convergence along an active LKF, there is no new ice formation and this mechanism is inoperative.

Figures 7-8 shows various surface and near-surface fields from our simulation for January 7th and 9th 2005. Note the presence of large vertical velocities and heat fluxes along a LKF extending across the Canada Basin. Large shear strain rates ( $\sim 1 \text{ day}^{-1}$ ) are coincident with large vertical ocean heat fluxes ( $200 \text{ W/m}^2$ ) at 40 m depth. This is in general agreement with observed deformations from RGPS and with in-situ observations from *McPhee et al.* [2005]. We note that anomalous vertical ocean heat fluxes are not present underneath some other active LKFs; compare, for instance, the shear strain rate or ice-



ocean stress curl with the vertical ocean heat flux in Figures 7-8 a,b,c. While anomalous ice-ocean stress curls consistently lead to anomalous vertical velocities, approximately half of the curls are negative; additionally, warmer water (or an NSTM) is not always present (see Figures 7-8 f).

To estimate how much of the simulated ocean heat flux is associated with the sea-ice divergence mechanism, we follow a similar approach to *Nguyen et al.* [2009] and estimate the amount of brine rejection in an open lead and the subsequent vertical ocean heat flux. For a typical winter sea-ice growth rate ( $dh/dt$ ) over a newly formed lead of 10 cm day<sup>-1</sup>, the amount of salt rejected per unit surface area is equal to  $\rho_i(S_{ml} - S_i)dh/dt$ ; here  $\rho_i$  (917 kg/m<sup>3</sup>) is the sea-ice density, and  $S_{ml}$  (30 psu) and  $S_i$  (6 psu) are the mixed-layer and ice salinities. This salt flux will be rejected in the form of highly saline brine waters. The brine volume flux per unit surface area,  $V_b$  can be estimated as:

$$\rho_b S_b \frac{d}{dt} V_b = \rho_i (S_{ml} - S_i) \frac{d}{dt} h, \quad (2)$$

where  $\rho_b$  and  $S_b$  are the brine water density and salinity. This brine volume will then mix with lower salinity mixed-layer water and feed the cold halocline layer [*Rudels et al.*, 1996]. Conservation of salt implies

$$\rho_b S_b \frac{d}{dt} V_b + \rho_{ml} S_{ml} \frac{d}{dt} V_{ml} = \rho_{chl} S_{chl} \frac{d}{dt} V_{chl} \quad (3)$$

and

$$V_{ml} + V_b = V_{chl}. \quad (4)$$

Here, the subscripts  $ml$  and  $chl$  stand for mixed layer and Cold Halocline Layer, respectively. Combining equations (2-4) gives

$$dV_{chl}/dt = \frac{\rho_i(S_{ml} - S_i)}{\rho_b S_b} \frac{(\rho_b S_b - \rho_{ml} S_{ml})}{(\rho_{chl} S_{chl} - \rho_{ml} S_{ml})} \frac{dh}{dt}. \quad (5)$$

In the above, we have assumed that the brine will mix with ambient mixed-layer water to a salinity that is equal to a typical mean CHL salinity of 29.5 psu. For an observed range of brine salinity between 42 and 92 psu [Wakatsuchi and Ono, 1983], and assuming a 1 °C temperature difference ( $\Delta T$ ) between the mixed-layer and the NSTM, we find that the implied ocean heat flux associated with brine convection,

$$F_{ocn}^{conv} = \rho_w C_{pw} V_{chl} \Delta T, \quad (6)$$

ranges from 10 to 43 W/m<sup>2</sup>. In other words, the vertical ocean heat flux associated with shallow convection is substantial, but it appears nonetheless to be considerably smaller than the values seen in our simulation or observations. We conclude that the large heat fluxes seen during the Jan. 7-9 event in our simulation are associated primarily with the Ekman pumping mechanism.

At the end of the January 7-9 event, surface winds relaxed and the LKF was no longer active, see Figure 9. The sustained vertical velocities of the previous 3 days were replaced by an alternation of positive and negative vertical velocities at regular intervals or about 10 hours. These are associated with inertia-gravity waves. The internal wave speed (derived from the slope of the v-shaped lines in Figure 9) is approximately 3.4 km/hr (or 0.94 m/s).

Comprend pas bien cette partie..

It is interesting to note that the vertical velocities associated with Ekman pumping beneath active sea ice leads extends to a depth of about 500 m (see Figure 10). That is, it extends through the cold halocline layer (where a large density gradient is present) and well into the Pacific and Atlantic layers. The associated vertical ocean heat flux is large immediately beneath the mixed-layer, at the location of the NSTM. As such, this process can be thought of as ventilating heat trapped beneath the mixed-layer after the previous

summer's melt season. It is also large in the Atlantic layer, where the ocean temperature is well above freezing. The maximum anomalous vertical velocity beneath the lead is  $3 \text{ m day}^{-1}$  of about 10 m over the course of a 3 day LKF event. This is of the same order of magnitude as that observed by *McPhee et al.* [2005] during the SHEBA campaign. Given the large vertical distance separating the Atlantic Layer from the surface, however, one cannot think of this Ekman pumping mechanism as tapping into this large heat source to melt ice. Instead, we propose that it allows heat to be brought up from the NSTM to the surface layer, making it available for ice melt.

That  $W$  extends well into the Atlantic Layer challenges the accepted view of the Arctic Ocean, whereby surface waters are mostly decoupled from the deeper Atlantic or Pacific waters, in which a large amount of heat is stored. The large heat fluxes discussed above take place along LKFs, where few measurements have been made for obvious logistical reasons. The heat flux beneath sea ice leads can be large, on the order of several hundreds of  $\text{W/m}^2$  [*McPhee et al.*, 2005, and Figure 10], and is very localized in time and space. We argue that the source of heat brought up to the surface along active LKFs by Ekman pumping is primarily heat from a previous summer trapped beneath the mixed layer - because of the small vertical distance ( 10 m) travelled by water during a lead event. Heat from the Atlantic or Pacific layer will also rise within the water column and excite internal gravity waves. Whether these waves will grow and break, causing mixing and retaining the heat at a higher level in the water column is beyond the scope of the present paper.

### Ouverture?

### 3.5. Implications for the sea ice mass balance

We next assess the spatial distribution of winter vertical heat fluxes related to Ekman pumping at active leads. To do this, we appeal to observations. Assuming warm water

is present immediately below the surface layer, the relevant heat flux is proportional to the curl of the ice-ocean stress. Neglecting the ocean current velocity in front of the ice velocity, this can be approximated as  $|\mathbf{U}_i|(\hat{\mathbf{z}} \cdot (\nabla \times \mathbf{U}_i))$ , where  $\mathbf{U}_i$  is the sea ice velocity. Results from a series of idealized experiments with spatial resolutions ranging from 100 m to 10 km and in which a discontinuity in the surface ice-ocean stress was imposed gives us confidence in this relationship (results not shown, and the subject of a subsequent paper). We thus take  $F_{ocn} \propto |\mathbf{U}_i|(\hat{\mathbf{z}} \cdot (\nabla \times \mathbf{U}_i))$ . The proportionality constant is obtained using the ice velocity curl and in-situ vertical ocean heat flux measured by *McPhee et al.* [2005]. Finally we assume a constant lead fraction of 1.5% [Kwok, 2010] and only consider grid cells with positive sea-ice velocity curl (see Figure 11).

Using the model described above and satellite-derived sea-ice drift and curl (from the Polar Path Finder [Fowler et al., 2013] and RGPS [<http://rkwok.jpl.nasa.gov/radarsat/>]), we infer  $F_{ocn}$ . The maximum values for the vertical ocean heat flux  $F_{ocn}$  are approximately 17 W/m<sup>2</sup> and are located along the Alaskan coast. Values around 5 W/m<sup>2</sup> are common off the Alaskan and Eurasian shelves, while over the Beaufort Sea, the mean value is around 1 W/m<sup>2</sup> (in the Figure 11, values are capped to emphasize structures away from the continental margin). These large heat fluxes are associated with the circum-Arctic flaw lead polynya, where large positive ice-velocity curls are often present between the landfast and mobile ice [Lukovich and Barber, 2005]. Note the distinct lines of higher vertical ocean heat fluxes north of Prince Patrick Island at the boundary between the dynamically active Beaufort Gyre and the sea ice north of the CAA. It is interesting that these are clearly visible even in a 12-year average.

These results are in general agreement with the vertical heat fluxes at the base of the mixed layer in our MITgcm simulations (e.g., compare Figures 5a,b and 11). They are also in agreement with [Yang *et al.*, 2004], who documented large upwelling event along the Alaskan coastline that extended below the halocline layer, associated with the passage of storms. Along the Alaskan and Chukchi Plateau shelf breaks, however, heat fluxes inferred as above are much smaller than those simulated by the MITgcm. This region is characterized by onshore geostrophic currents driven by the dominant northeasterly surface winds [Carmack and Chapman, 2003; Pickart *et al.*, 2013a, b]; these induce vertical heat fluxes which are not captured by the Ekman pumping calculation.

To infer ice growth anomalies, note that  $1 \text{ W/m}^2$  over an eight winter months corresponds to about 7 cm of ice loss. In the central Beaufort Sea, ice growth anomalies related to the Ekman pumping mechanism are small. Moreover, they are not cumulative from year to year due to a strong negative feedback (see for instance, *Tietsche et al.* [2011]). By contrast, the Ekman pumping mechanism appears to have a much more significant impact along and offshore from the shelfbreak. There, heat flux anomalies of around  $5 \text{ W/m}^2$  or larger would correspond to a reduced ice growth of over 35 cm over an eight winter months.

This, combined with the positive trend in summer ocean heat flux through Bering Strait [Woodgate *et al.*, 2012], the increased strength in the Beaufort Gyre since the 1990s [McPhee, 2013], and the positive trend in sea ice deformation in the Arctic [Rampal *et al.*, 2009], would result in a positive trend in vertical ocean heat flux and a negative trend in sea ice thickness along and offshore from the Alaskan shelfbreak. Thinner sea ice along and offshore of the Alaskan shelf break will melt earlier allowing the positive ice-albedo

feedback to kick in earlier in the season at a time when the sun is high above the horizon [Steele *et al.*, 2010; Perovich and Polashenski, 2012]. In turn, more ice melt in the western Arctic short-circuits the Beaufort Ice Gyre and provide a new mechanism for the loss of thick multi-year ice north of the CAA recirculating around the Beaufort Gyre [Steele *et al.*, 2011]. More first year ice also lead to larger area covered by melt ponds in late spring – early summer, lower surface albedo and increased summer melt [Perovich and Polashenski, 2012; Schröder *et al.*, 2014].

In the above analysis, we assumed the availability of a heat source such as the NSTM [Jackson *et al.*, 2010] or Pacific Summer Water [Spall *et al.*, 2008; Pickart *et al.*, 2013b] immediately beneath the mixed layer (Figure 12). The NSTM is clearly visible only in the Canada Basin; however, a heat source in the halocline layer is present in all four Basins (see for instance, Figures 7-8 f). To estimate the heat available, we consider the WOA dataset to calculate the integral of  $T - T_{fr}$  over a 150 m thick layer in the Canada Basin. This gives about  $3 \times 10^8 \text{ Jm}^{-2}$ . If we further assume this heat to be brought to the surface over an 8 month winter, the implied heat flux would be about  $14 \text{ W/m}^2$ . In other words, there appears to be more than enough heat lying immediately below the mixed layer to supply the fluxes inferred above for the Ekman pumping mechanism.

It may appear counterintuitive that there are a significant number of positive sea ice velocity curl LKFs in the western Arctic, i.e., given that this region is dominated by the anticyclonic Beaufort Gyre. Although the mean sea ice velocity curl is negative, the instantaneous curl can be either sign. Figures 13 (a,b) compare the winter average ice velocity curl and a similar average taken over positive values only. Figure 13 (c) shows the ice velocity curl PDF for the Beaufort Sea region, where LKFs are most active.

Large values are infrequent, but are skewed towards positive values along the Alaskan coastline. In the central Beaufort Gyre, the mean ice curl is negative; however, the standard deviation is large; for example, between 35 to 40% of LKFs have positive ice velocity curls in the central Beaufort Gyre and along the shelf break.

#### 4. Conclusion

Measurements of vertical ocean heat fluxes in the Arctic Ocean typically show very small values. Exceptions include locations where the cold halocline layer is absent, regions where large vertical mixing is induced by the bathymetry, and summer, when solar heat enters the mixed layer ocean through open water or thinner ice and causes under ice melt via turbulent fluxes. The general image of the Arctic Ocean is one in which sea ice and surface waters are largely decoupled from the deeper ocean because of the strong surface stratification induced by river runoff and sea ice melt and the presence of a cold halocline layer that buffers the surface waters from warmer waters below. Three main sources of heat lying beneath the Arctic Ocean mixed layer are as follows: 1- relic solar heat from the previous summer that was not ventilated during the fall (called the Near Surface Temperature Maximum); 2- Pacific summer waters that enter the Arctic Ocean through the Bering Strait, circulate eastward as a boundary current along the Alaskan coastline, and break off from the shelf into the interior of the Beaufort Gyre via eddies or in association with off-shore winds [Spall *et al.*, 2008; Pickart *et al.*, 2013b]; 3- Atlantic waters that enter the Arctic through the West Spitsbergen Current or the Barents Sea gate, circulate counterclockwise around the Arctic as a boundary current along the shelf break and shed eddies that bring these Atlantic waters to the interior of the four major Arctic Basins. We argue that this view of the Arctic is biased by the fact that most

observations are collected from platforms or instruments deployed at the center of floes and away from dynamical regions such as sea-ice leads, as is necessary for obvious logistic reasons. During the SHEBA campaign, the first measurements of the vertical ocean heat flux in the vicinity of an active sea ice leads was made [McPhee *et al.*, 2005]. Ocean heat fluxes as large as  $380 \text{ W/m}^2$  at 9 m depth were observed during this event. McPhee and colleagues argued that this heat was brought up to the surface by Ekman pumping associated with the curl of the ice-ocean surface stresses along an active Linear Kinematic Feature (LKF). In this paper we have run a fully coupled high resolution (3.75 - 5.5 km) ice-ocean model forced with reanalysis atmospheric fields, in order to test this hypothesis.

Our simulations show large vertical velocities extending far into the Atlantic layer are indeed found along active LKFs. When the surface ice-ocean surface stress curl is positive, this implies an upward advective transport of heat. By far the largest vertical ocean heat fluxes simulated by the model are located along the flaw lead polynya [Lukovich and Barber, 2005], particularly along and offshore of the Alaskan shelf break and Chukchi Plateau. There, vertical advective heat flux the order of a few  $100 \text{ W/m}^2$  are common. In the interior of the Beaufort Gyre (Amerasian Basin), this is reduced to only a few  $\text{W/m}^2$  when averaged over several winters. Since the mechanism relies on a positive sea-ice velocity curl, and this region is dominated by negative wind stress curls, it may seem counter-intuitive that this mechanism would produce any upward heat flux. The apparent contradiction is resolved when one takes into account the considerable spread about the mean in sea ice velocity curl.

The simulated mean vertical ocean heat flux is in accord with an observation-based estimate using satellite-derived sea ice drift speed and curl (RGPS) and using the one



observations by *McPhee et al.* [2005] as an anchor point. In the Eurasian Basin, the magnitude of the mean vertical ocean heat flux is similar to that of the Amerasian Basin. The simulated vertical velocities under active sea ice leads are of the order of  $10 \text{ m day}^{-1}$  (in accord with observations by *McPhee et al.* [2005]) and last for the time of an active LKF event, typically a few days. For this reason, we suggest that — despite the fact that anomalous vertical velocity beneath active LKFs extend well into the Atlantic Layer ( 500 m) — the source of the heat brought up in the mixed-layer is more likely the warmer waters of the NSTM - in accord with *McPhee et al.* [2005] hypothesis. The rise of pycnoclines deep beneath the mixed layer associated with Ekman pumping also generates internal waves that travels away from the source beneath the active LKFs. Whether these waves will grow, break and leave heat higher in the water column (constituting a slow migration of Atlantic or Pacific heat in the water column) is beyond the scope of the present paper. Along and offshore of the Alaskan and Chukchi Plateau shelf break, the magnitude of the vertical ocean heat flux and vertical velocity is much larger and the source of the heat can be of summer Pacific origin.

We suggest that the large Ekman pumping velocities along and offshore from the Alaskan and Chukchi Plateau shelf break, together with the presence of a heat source associated with the Pacific water, could be responsible for the recent observations that sea ice loss in the western Arctic is earlier and more extensive than had been suggested by climate models, [*Comiso et al.*, 2008; *Comiso*, 2012; *Stroeve et al.*, 2007]. Moreover, as the sea ice cover thins, a more mobile ice pack should lead to an increase in the amplitude of this Ekman pumping mechanism and, presumably, a further acceleration of ice melt.

Future work will include idealized and realistic higher resolution coupled ice-ocean simulations using the Jacobian Free Newton Krylov solver [Lemieux et al., 2008]. This solver allows for the full convergence of the highly non-linear sea ice momentum equation, and consequently a better resolution of the discontinuity in the surface ice-ocean surface stress [Lemieux et al., 2010], the driver for large Ekman-driven vertical ocean heat fluxes.

**Acknowledgments.** Support for this work is provided in part by the Fonds de Recherche en Science du Climat (FRSCO) from the Ouranos Consortium, the Natural Sciences and Engineering Council (NSERC) Discovery Foundation, the Environment Canada Grants and Contribution program, the ArcticNet Operating Grant and by the Office of Naval Research (N000141110977). We acknowledge funding from the Natural Sciences and Engineering Research Council of Canadas Climate Change and Atmospheric Research initiative via the Canadian Sea Ice and Snow Evolution (CanSISE) Network. We are grateful to our colleagues from the JPL NASA (Dimitris Menemenlis, An Nguyen) and AWI (Martin Losch) for their help in setting up the model and data post-processing. We gratefully acknowledge Compute Canada for computing resources and support from the McGill University’s Centre for High Performance Computing. This project is a contribution to the research program of Quebec-Ocean.

## References

Aagaard, K., L. Coachman, and E. Carmack (1981), On the halocline of the arctic ocean, *Deep Sea Research Part A. Oceanographic Research Papers*, 28(6), 529 – 545, doi: 10.1016/0198-0149(81)90115-1.

- Arakawa, A., and V. Lamb (1977), Computational design of the basic dynamical processes of the ucla general circulation model, *Methods in Computational Physics*, *17*, 173–265.
- Bitz, C. M., M. M. Holland, E. C. Hunke, and R. E. Moritz (2005), Maintenance of the sea-ice edge, *Journal of Climate*, *18*, 2903–2921, doi:10.1175/JCLI3428.1.
- Carmack, E., and D. C. Chapman (2003), Wind-driven shelf/basin exchange on an arctic shelf: The joint roles of ice cover extent and shelf-break bathymetry, *Geophysical Research Letters*, *30*(14), doi:10.1029/2003GL017526, 1778.
- Comiso, J. C. (2006), Arctic warming signals from satellite observations, *Weather*, *61*(3), 70–76, doi:10.1256/wea.222.05.
- Comiso, J. C. (2012), Large decadal decline of the arctic multiyear ice cover, *Journal of Climate*, *25*(4), 1176–1193.
- Comiso, J. C., C. L. Parkinson, R. Gersten, and L. Stock (2008), Accelerated decline in the arctic sea ice cover, *Geophysical Research Letters*, *35*(1), L01,703, doi:10.1029/2007GL031972.
- Daru, V., and C. Tenaud (2004), High order one-step monotonicity-preserving schemes for unsteady compressible flow calculations, *Journal of Computational Physics*, *193*(2), 563 – 594, doi:10.1016/j.jcp.2003.08.023.
- Fowler, C., J. Maslanik, W. Emery, and M. Tschudi (2013), Polar pathfinder daily 25 km ease-grid sea ice motion vectors. version 2. [indicate subset used], *NASA National Snow and Ice Data Center Distributed Active Archive Center*.
- Hansen, J., M. Sato, R. Ruedy, K. Lo, D. W. Lea, and M. Medina-Elizade (2006), Global temperature change, *Proceedings of the National Academy of Sciences*, *103*(39), 14,288–14,293, doi:10.1073/pnas.0606291103.

- Hibler, W. D. (1979), A dynamic thermodynamic sea ice model, *J. Phys. Oceanogr.*, *9*, 815–846, doi:10.1175/1520-0485(1979)009<0815:ADTSIM>2.0.CO;2.
- Hibler, W. D. (1980), Modeling a variable thickness sea ice cover, *Mon. Wea. Rev.*, *1*, 1943–1973.
- Holland, M. M., C. M. Bitz, and B. Tremblay (2006), Future abrupt reductions in the summer arctic sea ice, *Geophysical Research Letters*, *33*(23), L23,503, doi:10.1029/2006GL028024.
- Huwald, H., L.-B. Tremblay, and H. Blatter (2005), Reconciling different observational data sets from surface heat budget of the arctic ocean (sheba) for model validation purposes, *Journal of Geophysical Research: Oceans*, *110*(C5), C05,009, doi:10.1029/2003JC002221.
- Jackett, D. R., and T. J. McDougall (1995), Minimal adjustment of hydrographic profiles to achieve static stability, *Journal of Atmospheric and Oceanic Technology*, *12*(2), 381–389, doi:10.1175/1520-0426(1995)012<0381:MAOHPT>3E2.0.CO;2.
- Jackson, J. M., E. C. Carmack, F. A. McLaughlin, S. E. Allen, and R. G. Ingram (2010), Identification, characterization, and change of the near-surface temperature maximum in the canada basin, 19932008, *Journal of Geophysical Research: Oceans*, *115*(C5), C05,021, doi:10.1029/2009JC005265.
- Jones, E. P., L. G. Anderson, and J. H. Swift (1998), Distribution of atlantic and pacific waters in the upper arctic ocean: Implications for circulation, *Geophysical Research Letters*, *25*(6), 765–768, doi:10.1029/98GL00464.
- Kay, J. E., M. M. Holland, and A. Jahn (2011), Inter-annual to multi-decadal arctic sea ice extent trends in a warming world, *Geophysical Research Letters*, *38*(15), L15,708,

doi:10.1029/2011GL048008, 115708.

Krishfield, R. A., and D. K. Perovich (2005), Spatial and temporal variability of oceanic heat flux to the arctic ice pack, *J. Geophys. Res.*, *110*, C07,021, doi:10.1029/2004JC002293.

Kwok, R. (2010), Satellite remote sensing of sea-ice thickness and kinematics: a review, *Journal of Glaciology*, *56*(200), 1129–1140, doi:doi:10.3189/002214311796406167.

Lammers, R. B., A. I. Shiklomanov, C. J. Vrmsmarty, B. M. Fekete, and B. J. Peterson (2001), Assessment of contemporary arctic river runoff based on observational discharge records, *J. Geophys. Res.*, *106*, 3321–3334, doi:10.1029/2000JD900444.

Large, W. G., J. C. McWilliams, and S. C. Doney (1994), Oceanic vertical mixing: A review and a model with a nonlocal boundary layer parameterization, *Rev. Geophys.*, *32*, 363–403, doi:10.1029/94RG01872.

Lei, R., N. Li, P. Heil, B. Cheng, Z. Zhang, and B. Sun (2014), Multiyear sea ice thermal regimes and oceanic heat flux derived from an ice mass balance buoy in the arctic ocean, *Journal of Geophysical Research: Oceans*, *119*(1), 537–547, doi:10.1002/2012JC008731.

Lemieux, J.-F., B. Tremblay, S. Thomas, J. Sedlasek, and L. A. Mysak (2008), Numerical convergence of viscous-plastic sea ice models, *J. Geophys. Res.*, *113*, C10,004, doi:10.1029/2007JC004680.

Lemieux, J.-F., B. Tremblay, J. Sedlasek, P. Tupper, S. Thomas, D. Huard, and J.-P. Auclair (2010), Improving the numerical convergence of viscous-plastic sea ice models with the jacobian-free newton-krylov method, *Journal of Computational Physics*, *229*(8), 2840 – 2852, doi:10.1016/j.jcp.2009.12.011.

- Lind, S., and R. B. Ingvaldsen (2012), Variability and impacts of atlantic water entering the barents sea from the north, *Deep Sea Research Part I: Oceanographic Research Papers*, *62*(0), 70 – 88, doi:10.1016/j.dsr.2011.12.007.
- Lukovich, J. V., and D. G. Barber (2005), On sea ice concentration anomaly coherence in the southern beaufort sea, *Geophysical Research Letters*, *32*(10), L10,705, doi:10.1029/2005GL022737.
- Marshall, J., A. Adcroft, C. Hill, L. Perelman, and C. Heisey (1997a), A finite-volume, incompressible navier stokes model for studies of the ocean on parallel computers, *J. Geophys. Res.*, *102*, 5753–5766, doi:10.1029/96JC02775.
- Marshall, J., C. Hill, L. Perelman, and C. Heisey (1997b), Hydrostatic, quasi-hydrostatic, and nonhydrostatic ocean modeling, *J. Geophys. Res.*, *102*, 5733–5752, doi:10.1029/96JC02776.
- Maykut, G. A., and M. G. McPhee (1995), Solar heating of the arctic mixed layer, *J. Geophys. Res.*, *100*, 24,691–24,703, doi:10.1029/95JC02554.
- Maykut, G. A., and D. K. Perovich (1987), The role of shortwave radiation in the summer decay of a sea ice cover, *J. Geophys. Res.*, *92*, 7032–7044, doi:10.1029/JC092iC07p07032.
- Maykut, G. A., and N. Untersteiner (1971), Some results from a time-dependent thermodynamic model of sea ice, *J. Geophys. Res.*, *76*, 1550–1575, doi:10.1029/JC076i006p01550.
- McLaughlin, F. A., E. C. Carmack, W. J. Williams, S. Zimmermann, K. Shimada, and M. Itoh (2009), Joint effects of boundary currents and thermohaline intrusions on the warming of atlantic water in the canada basin, 19932007, *Journal of Geophysical Research: Oceans*, *114*(C1), C00A12, doi:10.1029/2008JC005001.

- McPhee, M. G. (2013), Intensification of geostrophic currents in the Canada basin, arctic ocean, *Journal of Climate*, *26*(10), 3130 – 3138, doi:10.1175/JCLI-D-12-00289.1.
- McPhee, M. G., T. Kikuchi, J. H. Morison, and T. P. Stanton (2003), Ocean-to-ice heat flux at the north pole environmental observatory, *Geophysical Research Letters*, *30*(24), 2274, doi:10.1029/2003GL018580.
- McPhee, M. G., R. Kwok, R. Robins, and M. Coon (2005), Upwelling of arctic pycnocline associated with shear motion of sea ice, *Geophys. Res. Lett.*, *32*, L10,616, doi:10.1029/2004GL021819.
- Menemenlis, D., I. Fukumori, and T. Lee (2005), Using green's functions to calibrate an ocean general circulation model, *Monthly Weather Review*, *133*, 1224–1240, doi:10.1175/MWR2912.1.
- Morison, J. (1980), Forced internal waves in the arctic ocean, Phd thesis, Dept. of Geophysics, Univ. of Wash., Seattle.
- Morison, J., K. Aagaard, and M. Steele (2000), Recent environmental changes in the arctic: A review, *ARCTIC*, *53*(4).
- Nguyen, A. T., D. Menemenlis, and R. Kwok (2009), Improved modeling of the arctic halocline with a subgrid-scale brine rejection parameterization, *J. Geophys. Res.*, *114*, C11,014, doi:10.1029/2008JC005121.
- Notz, D., M. G. McPhee, M. G. Worster, G. A. Maykut, K. H. Schlunzen, and H. Eicken (2003), Impact of underwater-ice evolution on arctic summer sea ice, *Journal of Geophysical Research: Oceans*, *108*(C7), 3223, doi:10.1029/2001JC001173.
- Perovich, D. K., and B. Elder (2002), Estimates of ocean heat flux at sheba, *Geophysical Research Letters*, *29*(9), 58–1–58–4, doi:10.1029/2001GL014171.

- Perovich, D. K., and C. Polashenski (2012), Albedo evolution of seasonal arctic sea ice, *Geophysical Research Letters*, *39*(8), L08,501, doi:10.1029/2012GL051432.
- Perovich, D. K., T. C. Grenfell, J. A. Richter-Menge, B. Light, W. B. Tucker, and H. Eicken (2003), Thin and thinner: Sea ice mass balance measurements during sheba, *Journal of Geophysical Research: Oceans*, *108*(C3), 8050, doi:10.1029/2001JC001079.
- Pickart, R. S., L. M. Schulze, G. Moore, M. A. Charette, K. R. Arrigo, G. van Dijken, and S. L. Danielson (2013a), Long-term trends of upwelling and impacts on primary productivity in the alaskan beaufort sea, *Deep Sea Research Part I: Oceanographic Research Papers*, *79*(0), 106 – 121, doi:http://dx.doi.org/10.1016/j.dsr.2013.05.003.
- Pickart, R. S., M. A. Spall, and J. T. Mathis (2013b), Dynamics of upwelling in the alaskan beaufort sea and associated shelfbasin fluxes, *Deep Sea Research Part I: Oceanographic Research Papers*, *76*(0), 35 – 51, doi:http://dx.doi.org/10.1016/j.dsr.2013.01.007.
- Polyakov, I. V., L. A. Timokhov, V. A. Alexeev, S. Bacon, I. A. Dmitrenko, L. Fortier, I. E. Frolov, J.-C. Gascard, E. Hansen, V. V. Ivanov, S. Laxon, C. Mauritzen, D. Perovich, K. Shimada, H. L. Simmons, V. T. Sokolov, M. Steele, and J. Toole (2010), Arctic ocean warming contributes to reduced polar ice cap, *Journal of Physical Oceanography*, *40*, 2743–2756, doi:10.1175/2010JPO4339.1.
- Polyakov, I. V., V. A. Alexeev, I. M. Ashik, S. Bacon, A. Beszczynska-Mller, E. C. Carmack, I. A. Dmitrenko, L. Fortier, J.-C. Gascard, E. Hansen, J. Hlemann, V. V. Ivanov, T. Kikuchi, S. Kirillov, Y.-D. Lenn, J. McLaughlin, Fiona A. and Piechura, I. Repina, L. A. Timokhov, W. Walczowski, and R. Woodgate (2011), Fate of early 2000s arctic warm water pulse, *Bulletin of the American Meteorological Society*, *92*, 561–566, doi:10.1175/2010BAMS2921.1.



- Rampal, P., J. Weiss, and D. Marsan (2009), Positive trend in the mean speed and deformation rate of arctic sea ice, 1979-2007, *J. Geophys. Res.*, *114*, C05,013, doi:10.1029/2008JC005066.
- Rudels, B., L. G. Anderson, and E. P. Jones (1996), Formation and evolution of the surface mixed layer and halocline of the arctic ocean, *J. Geophys. Res.*, *101*, 8807–8821, doi:10.1029/96JC00143.
- Rudels, B., E. P. Jones, U. Schauer, and P. Eriksson (2004), Atlantic sources of the arctic ocean surface and halocline waters, *Polar Research*, *23*, 181–208, doi:10.1111/j.1751-8369.2004.tb00007.x.
- Schauer, U., E. Fahrbach, S. Osterhus, and G. Rohardt (2004), Arctic warming through the fram strait: Oceanic heat transport from 3 years of measurements, *Journal of Geophysical Research: Oceans*, *109*(C6), C06,026, doi:10.1029/2003JC001823.
- Schröder, D., D. L. Feltham, D. Flocco, and M. Tsamados (2014), September arctic sea-ice minimum predicted by spring melt-pond fraction, *Nature Climate Change*, *4*(5), 353 – 357, doi:10.1038/nclimate2203.
- Serreze, M. C., J. E. Walsh, F. S. Chapin III, T. Osterkamp, M. Dyurgerov, V. Romanovsky, W. C. Oechel, J. Morison, T. Zhang, and R. G. Barry (2000), Observational evidence of recent change in the northern high-latitude environment, *Climatic Change*, *46*(1/2), 159–207.
- Serreze, M. C., A. P. Barrett, A. G. Slater, M. Steele, J. Zhang, and K. E. Trenberth (2007), The large-scale energy budget of the arctic, *Journal of Geophysical Research: Atmospheres*, *112*(D11), D11,122, doi:10.1029/2006JD008230.

- Shaw, W. J., T. P. Stanton, M. G. McPhee, J. H. Morison, and D. G. Martinson (2009), Role of the upper ocean in the energy budget of arctic sea ice during sheba, *Journal of Geophysical Research: Oceans*, *114*(C6), C06,012, doi:10.1029/2008JC004991.
- Shimada, K., F. McLaughlin, E. Carmack, A. Proshutinsky, S. Nishino, and M. Itoh (2004), Trends in arctic sea ice extent from cmip5, cmip3 and observations, *Geophys. Res. Lett.*, *31*, L20,301, doi:10.1029/2004GL020860.
- Spall, M. A., R. S. Pickart, P. S. Fratantoni, and A. J. Plueddemann (2008), Western arctic shelfbreak eddies: Formation and transport, *J. Phys. Oceanogr.*, *38*(8), 1644–1668, doi:10.1175/2007JPO3829.1.
- Steele, M., and T. Boyd (1998), Retreat of the cold halocline layer in the arctic ocean, *J. Geophys. Res.*, *103*, 10,419–10,435, doi:10.1029/98JC00580.
- Steele, M., J. Zhang, and W. Ermold (2010), Mechanisms of summertime upper arctic ocean warming and the effect on sea ice melt, *Journal of Geophysical Research: Oceans*, *115*(C11), C11,004, doi:10.1029/2009JC005849.
- Steele, M., W. Ermold, and J. Zhang (2011), Modeling the formation and fate of the near-surface temperature maximum in the canadian basin of the arctic ocean, *Journal of Geophysical Research: Oceans*, *116*(C11), C11,015, doi:10.1029/2010JC006803.
- Stroeve, J., M. M. Holland, W. Meier, T. Scambos, and M. Serreze (2007), Arctic sea ice decline: Faster than forecast, *Geophys. Res. Lett.*, *34*, L09,501, doi:10.1029/2007GL029703.
- Stroeve, J. C., V. Kattsov, A. Barrett, M. Serreze, T. Pavlova, M. Holland, and W. N. Meier (2012), Trends in arctic sea ice extent from cmip5, cmip3 and observations, *Geophys. Res. Lett.*, *39*, L16,502, doi:10.1029/2012GL052676.

- Sundfjord, A., I. Fer, Y. Kasajima, and H. Svendsen (2007), Observations of turbulent mixing and hydrography in the marginal ice zone of the barents sea, *Journal of Geophysical Research: Oceans*, *112*(C5), C05,008, doi:10.1029/2006JC003524.
- Tietsche, S., D. Notz, J. H. Jungclauss, and J. Marotzke (2011), Recovery mechanisms of arctic summer sea ice, *Geophysical Research Letters*, *38*(2), L02,707, doi:10.1029/2010GL045698.
- Timmermans, M.-L., J. Toole, R. Krishfield, and P. Winsor (2008), Ice-tethered profiler observations of the double-diffusive staircase in the canada basin thermocline, *J. Geophys. Res.*, *113*, C00A02, doi:10.1029/2008JC004829.
- Uotila, P., D. M. Holland, M. A. Morales Maqueda, S. Hkkinen, G. Holloway, M. Karcher, F. Kauker, M. Steele, N. Yakovlev, J. Zhang, and A. Proshutinsky (2006), An energy-diagnostics intercomparison of coupled ice-ocean arctic models, *Ocean Modelling*, *11*(12), 1 – 27, doi:http://dx.doi.org/10.1016/j.ocemod.2004.11.003.
- Wakatsuchi, M., and N. Ono (1983), Measurements of salinity and volume of brine excluded from growing sea ice, *Journal of Geophysical Research: Oceans*, *88*(C5), 2943–2951, doi:10.1029/JC088iC05p02943.
- Woodgate, R. A., K. Aagaard, R. D. Muench, J. Gunn, G. Bjrk, B. Rudels, A. Roach, and U. Schauer (2001), The arctic ocean boundary current along the eurasian slope and the adjacent lomonosov ridge: Water mass properties, transports and transformations from moored instruments, *Deep Sea Research Part I: Oceanographic Research Papers*, *48*(8), 1757 – 1792, doi:http://dx.doi.org/10.1016/S0967-0637(00)00091-1.
- Woodgate, R. A., T. J. Weingartner, and R. Lindsay (2012), Observed increases in bering strait oceanic fluxes from the pacific to the arctic from 2001 to 2011 and their impacts

on the arctic ocean water column, *Geophysical Research Letters*, 39(24), L24,603, doi:10.1029/2012GL054092.

Yang, J., J. Comiso, D. Walsh, R. Krishfield, and S. Honjo (2004), Storm-driven mixing and potential impact on the arctic ocean, *Journal of Geophysical Research: Oceans*, 109(C4), C04,008, doi:10.1029/2001JC001248.

Zhang, J., and W. D. Hibler (1997), On an efficient numerical method for modeling sea ice dynamics, *J. Geophys. Res.*, 102, 8691–8702, doi:10.1029/96JC03744.

**Table 1.** Model parameters

Name	Symbol	Value
Albedo Ocean	$\alpha_o$	0.1556
Albedo Dry Ice	$\alpha_i$	0.7
Ocean Density	$\rho_w$	1027.5 kg/m <sup>3</sup>
Ice density	$\rho_i$	910 kg/m <sup>3</sup>
Freezing temperature	$T_{fr}$	-1.7348 °C
Specific heat	$C_{pw}$	3974 Jkg <sup>-1</sup> K <sup>-1</sup>
Ocean Emissivity	$\epsilon_o$	0.97
Stefan-Boltzman constant	$\sigma$	5.67 x 10 <sup>-8</sup> W m <sup>-2</sup> K <sup>-4</sup>

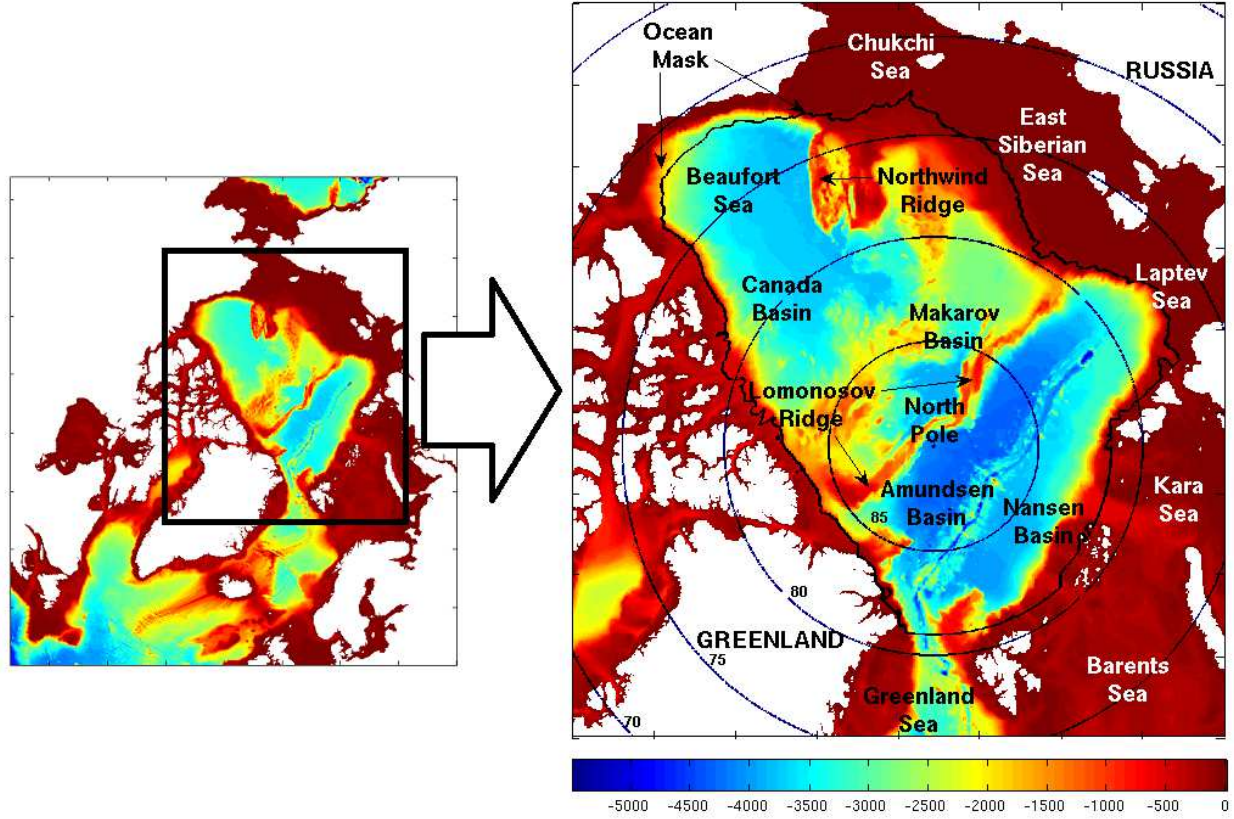


**Figure 1.** Model domain for the regional MITgcm (left panel). Zoom-in of the region of interest for the present study, including key regions and geological features referred to the text (right panel). The bottom ocean topography is shown below the right panel (in meter). The mask used to calculate all mean quantities presented in the result section is shown as a thick black line in right panel. This mask includes all depths  $> 300$  m, except in the Nansen Basin where it is based on a latitude circle.

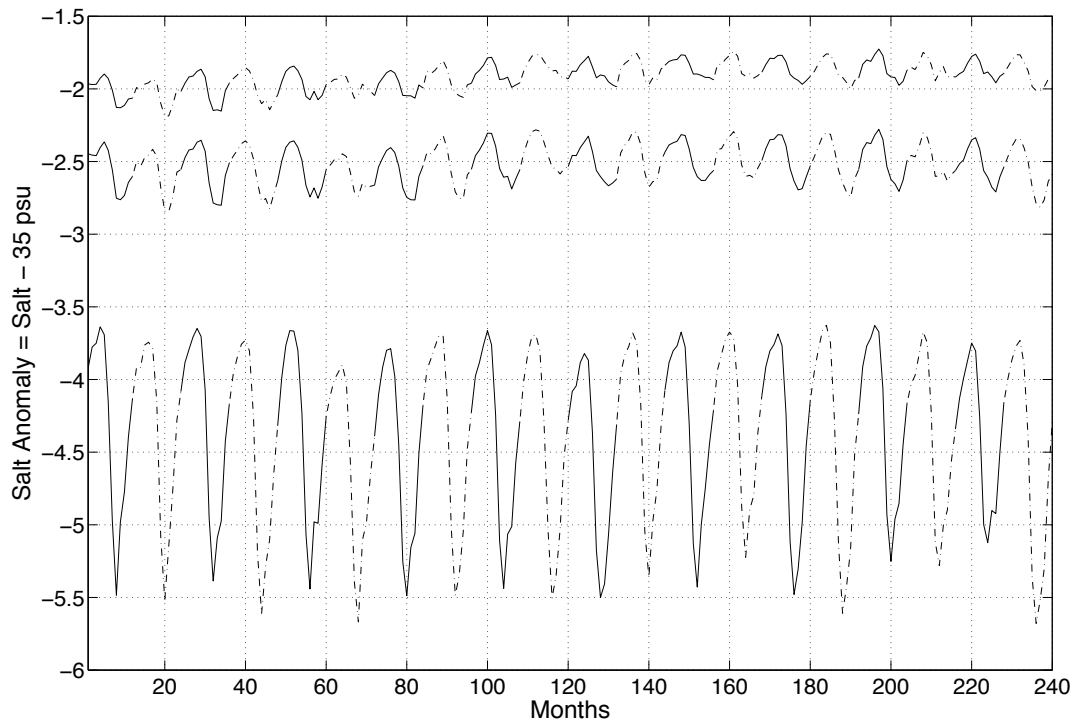


**Figure 2.** Seasonal cycle of the domain-averaged monthly mean fresh water content in the first 10 (bottom curve), 100 (middle curve) and 207 (top curve) meters of the Arctic Ocean. Solid and dash-dotted lines represent separate years.

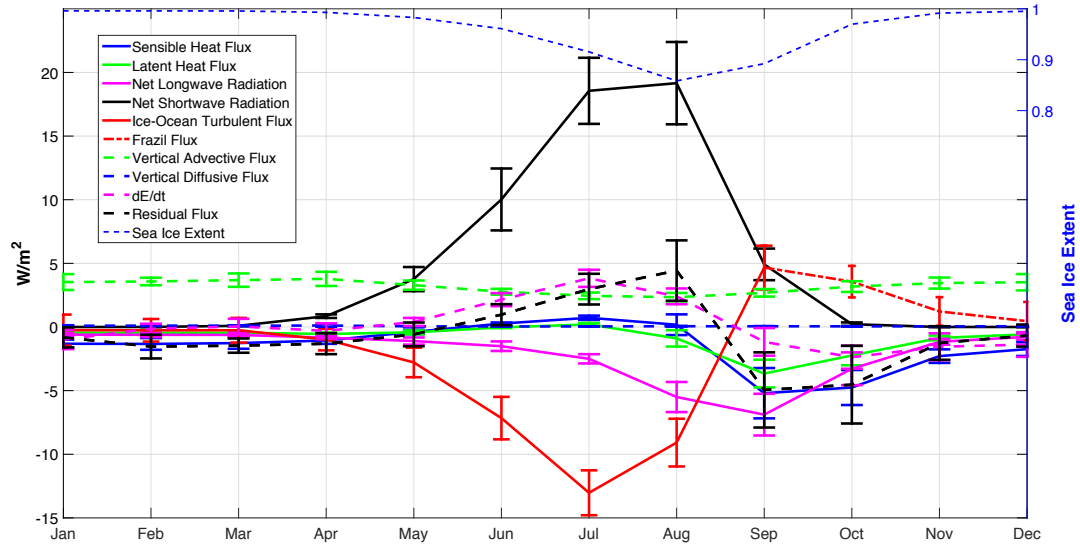


**Figure 3.** The seasonal cycle of the monthly mean (10-year average) radiative and turbulent heat fluxes, tendency term (left axis) and sea ice extent (right axis).

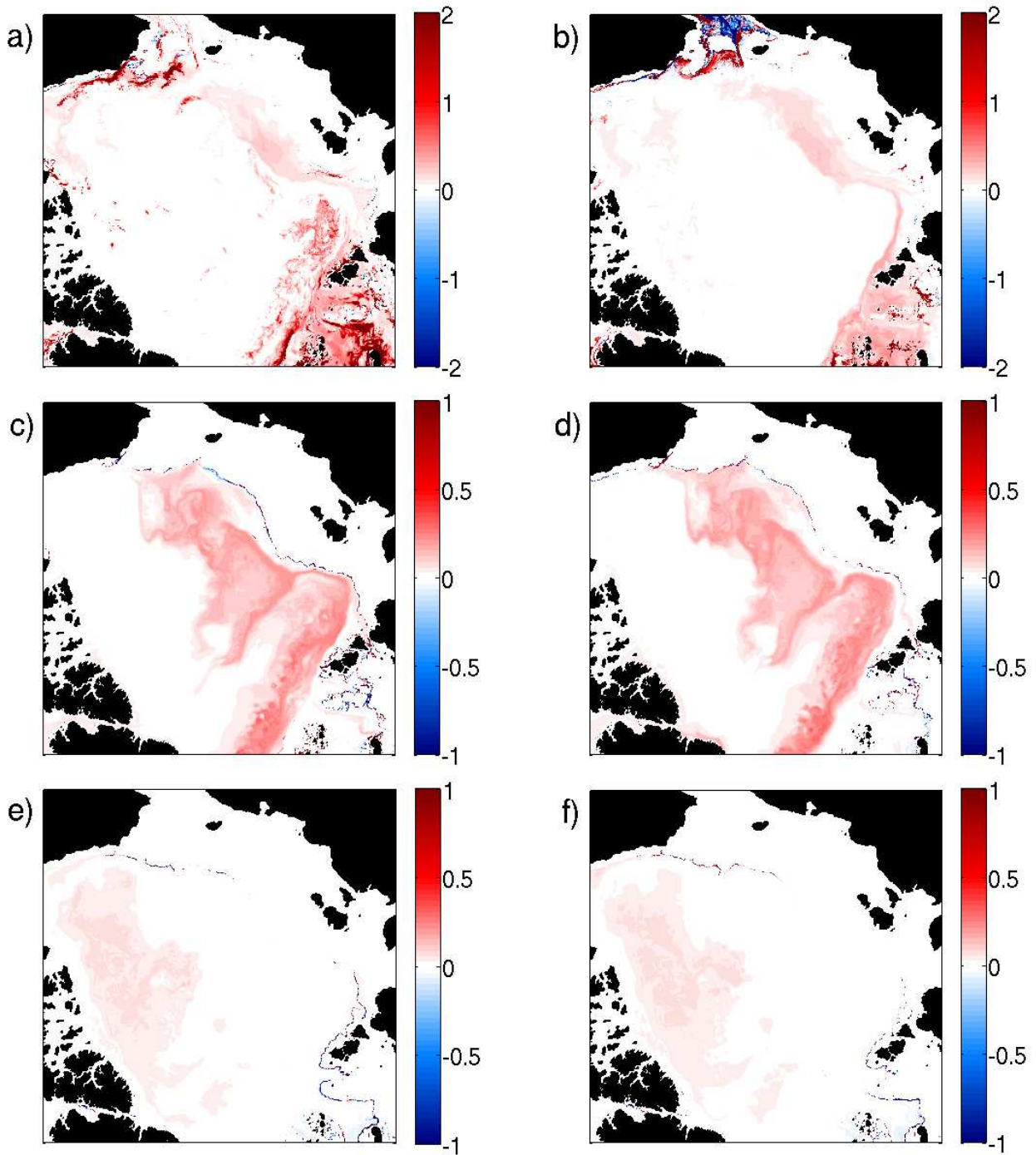


**Figure 4.** Averaged winter DJF (a,c,e) and summer JJA (b,d,f) vertical diffusive fluxes ( $\text{W}/\text{m}^2$ ) at 40 m (a,b), 100 m (c,d) and 207 m (e,f). The colorbars are capped at  $2 \text{ W}/\text{m}^2$  (panel a,b) and at  $1 \text{ W}/\text{m}^2$  (panel c,d,e,f).



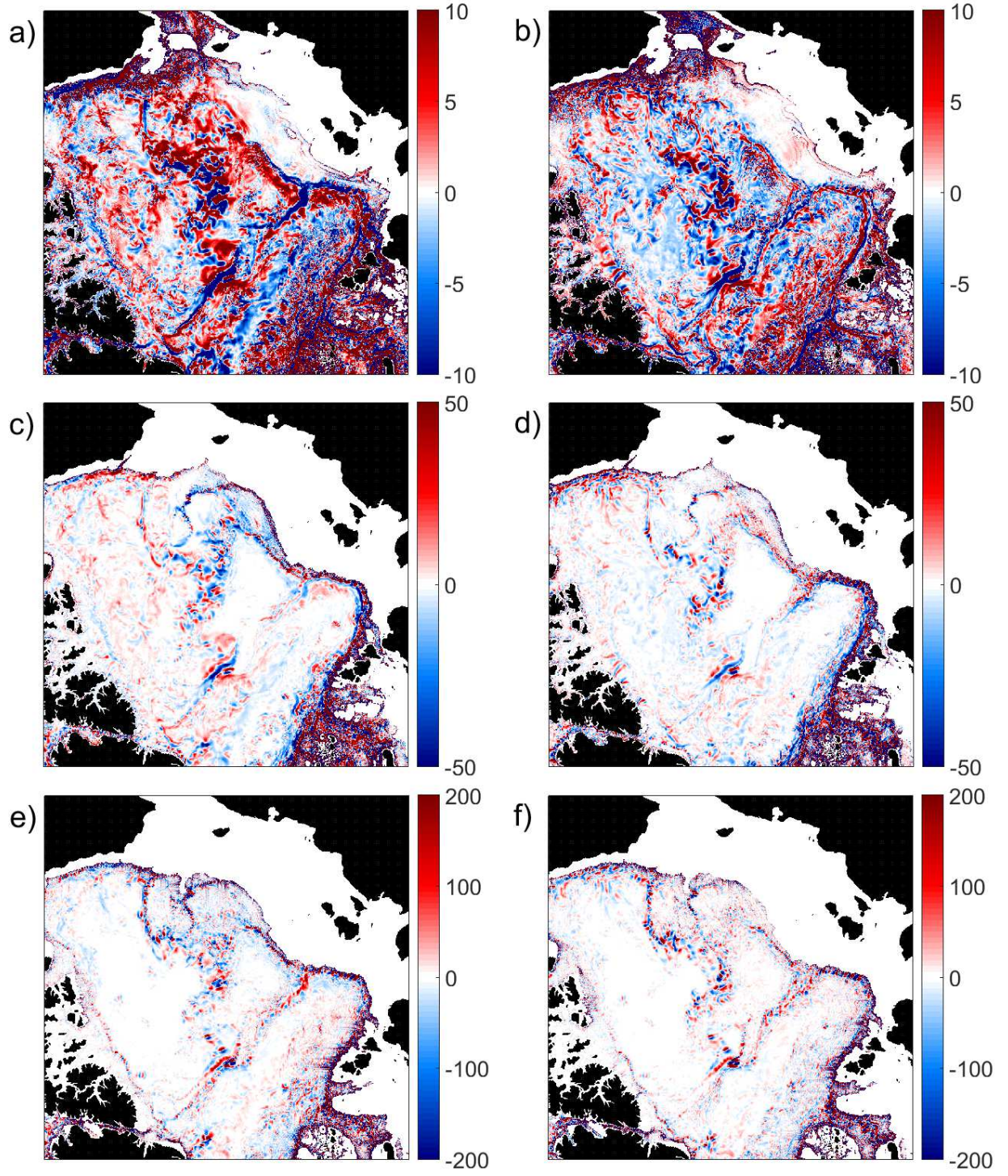


**Figure 5.** Averaged winter DJF (a,c,e) and summer JJA (b,d,f) vertical advective fluxes ( $W/m^2$ ) at 40 m (a,b), 100 m (c,d) and 207 m (e,f). The colorbars are capped at 10, 50 and 200  $W/m^2$  respectively.

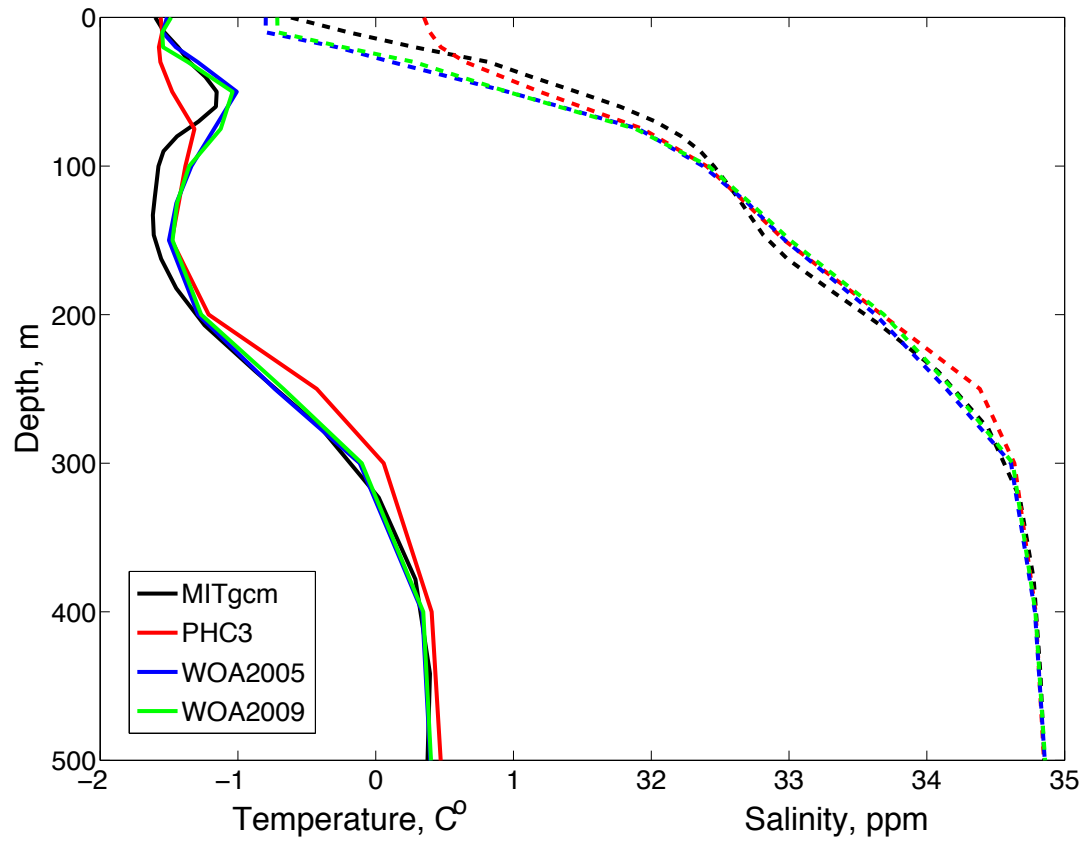


**Figure 6.** Vertical profiles of temperature and salinity in the Canada Basin in January 1983 of simulation. Black line - MITgcm result, red - PHC3 climatology, blue - WOA2005 climatology and green - WOA2009 climatology.



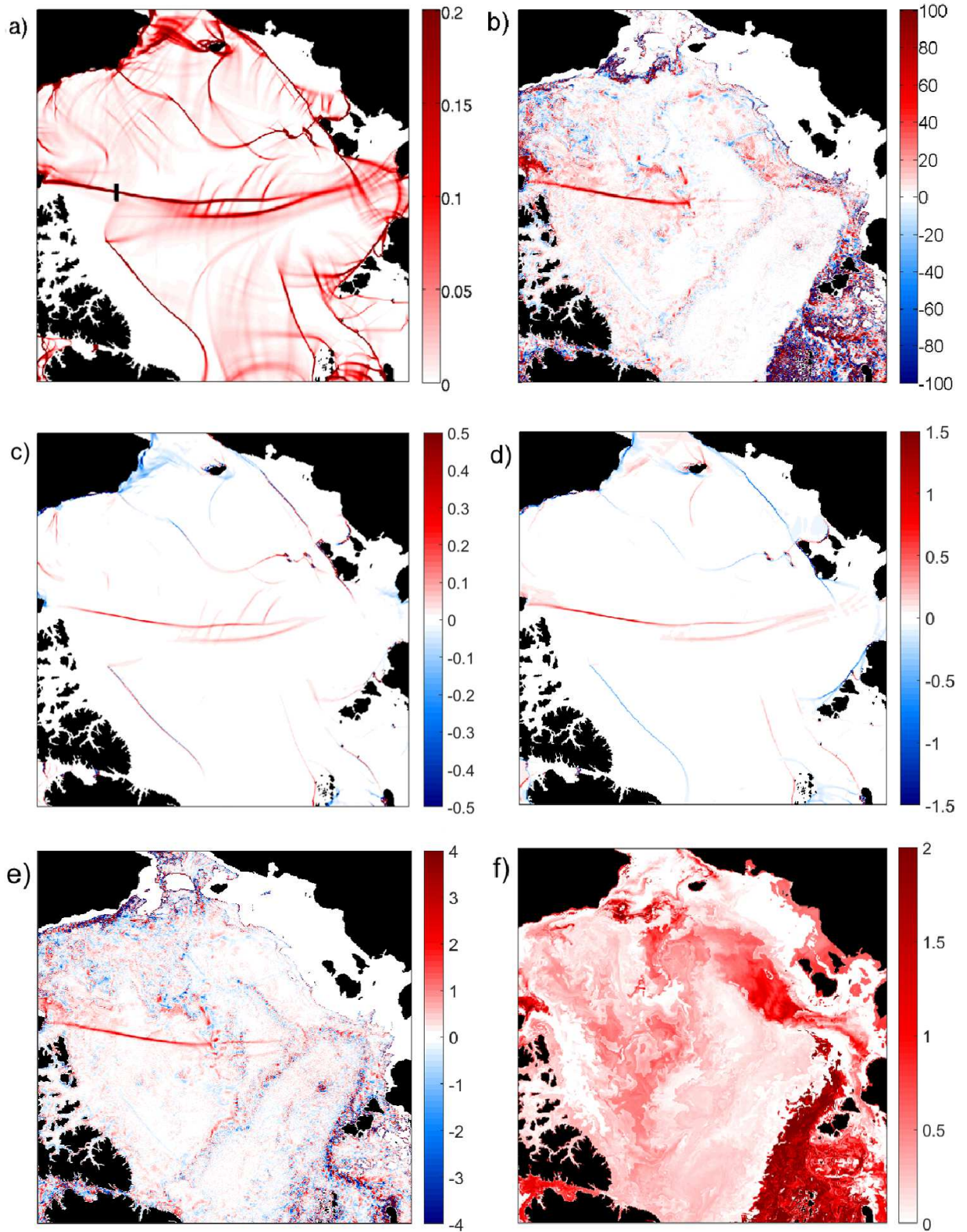


**Figure 7.** (a) January 7th, 2005. Spatial distribution of sea-ice shear strain rate ( $day^{-1}$ ), (b) vertical advective ocean heat flux ( $W/m^2$ ) at 40 m depth, (c) sea-ice stress curl ( $day^{-1}$ ), (d) sea-ice divergence ( $day^{-1}$ ), (e) vertical velocity ( $m/day$ ) and (f) temperature difference between D R A F T August 13, 2015, 5:35pm D R A F T maximum temperature in NSTM and the mixed layer temperature. The shear strain rate in (a) are capped at  $0.2 day^{-1}$  to show leads with small and large strain rates.

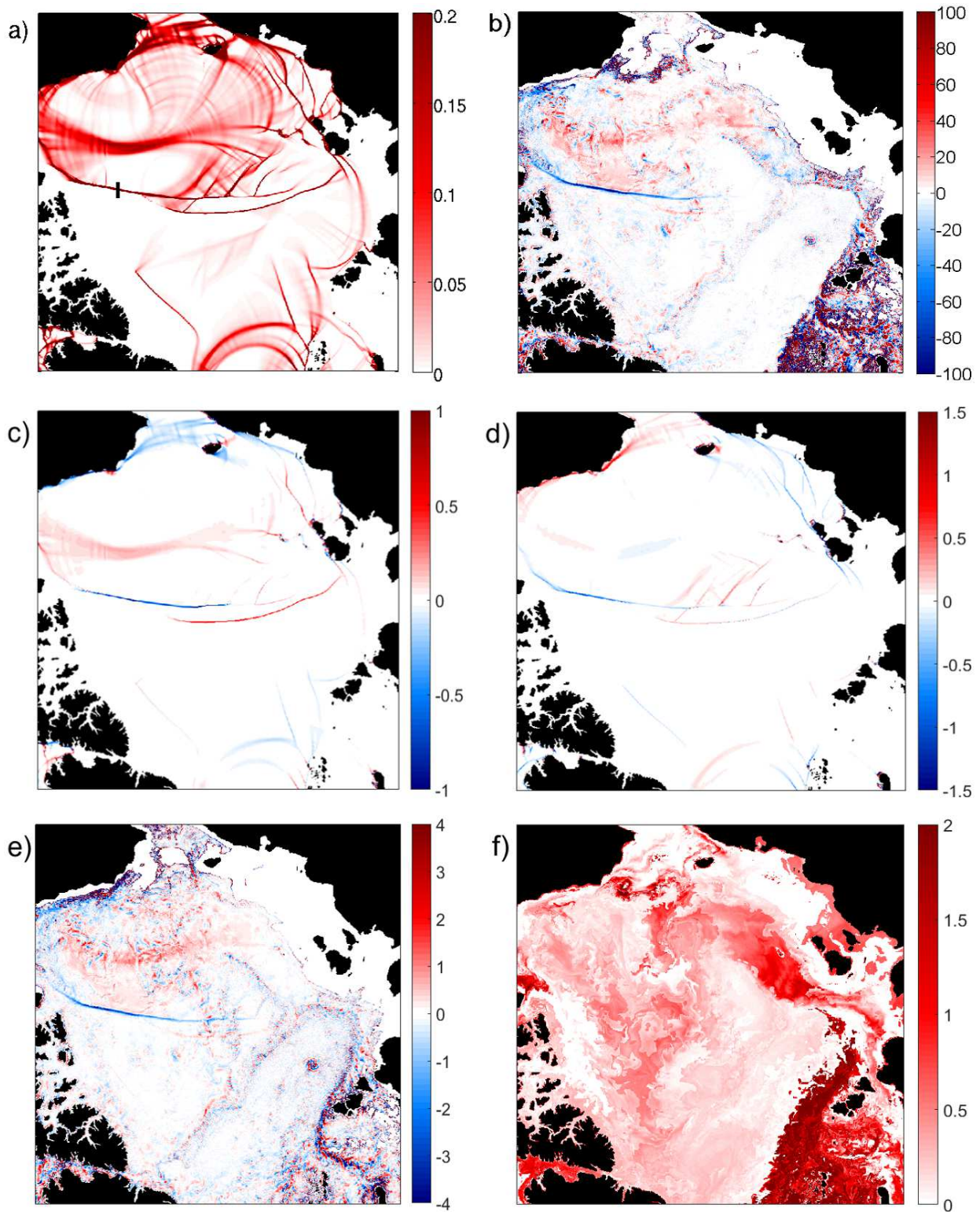


**Figure 8.** (a) January 9th, 2005. Spatial distribution of sea-ice shear strain rate ( $day^{-1}$ ), (b) vertical advective ocean heat flux ( $W/m^2$ ) at 40 m depth, (c) sea-ice stress curl ( $day^{-1}$ ), (d) sea-ice divergence ( $day^{-1}$ ), (e) vertical velocity ( $m/day$ ) and (f) Temperature difference between maximum temperature in NSTM and the mixed layer temperature. The shear strain rate in (a) are capped at  $0.2 day^{-1}$  to show leads with small and large strain rates.



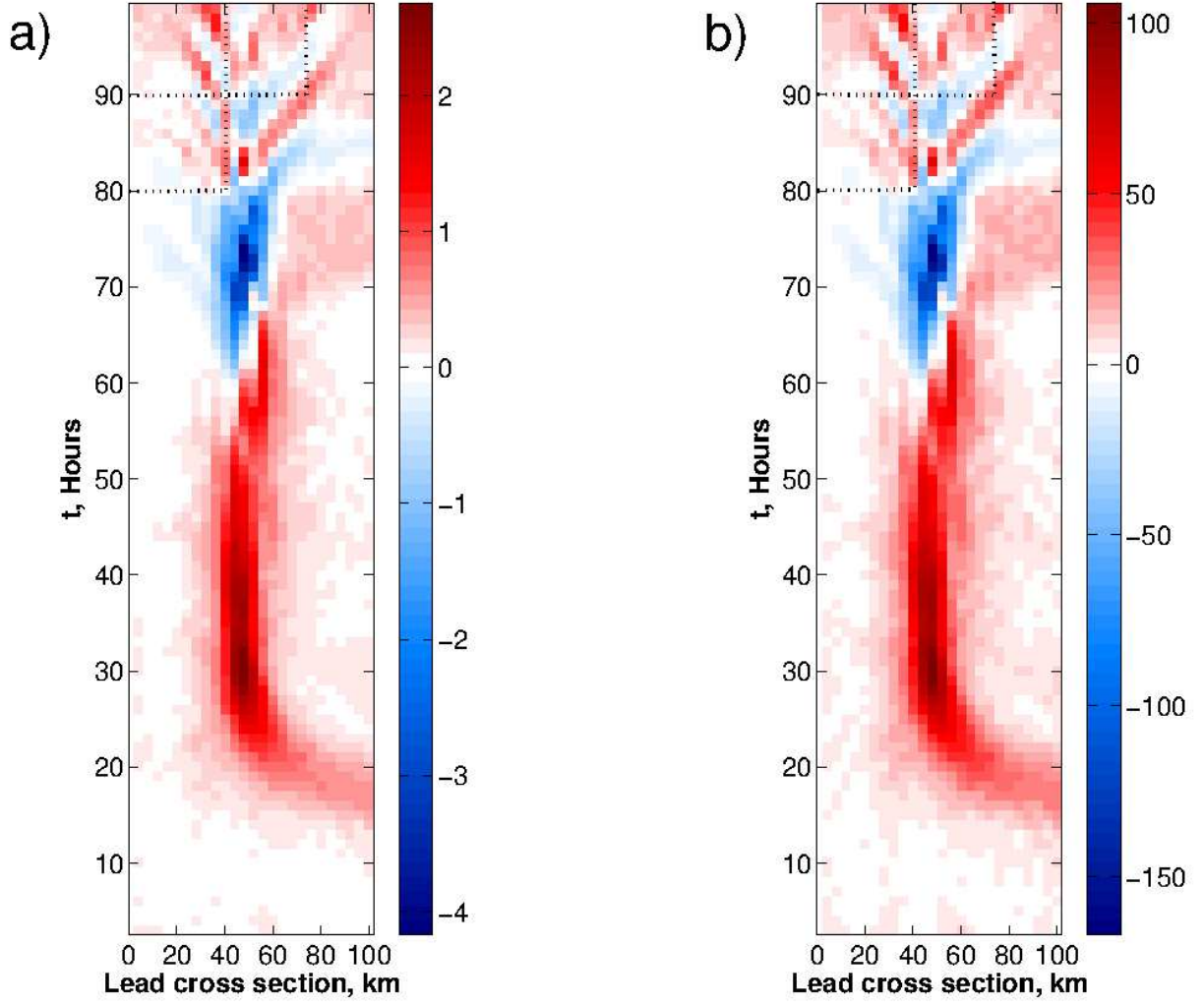


**Figure 9.** (a) Hovmuller diagram of the vertical velocity (m/day) and (b) vertical advective ocean heat flux ( $\text{W/m}^2$ ) at 40 m depth for January 7, 6:00 to January 9, 18:00, 2005, along the cross section shown on Figures 7-8 panel (a) (thick black line).

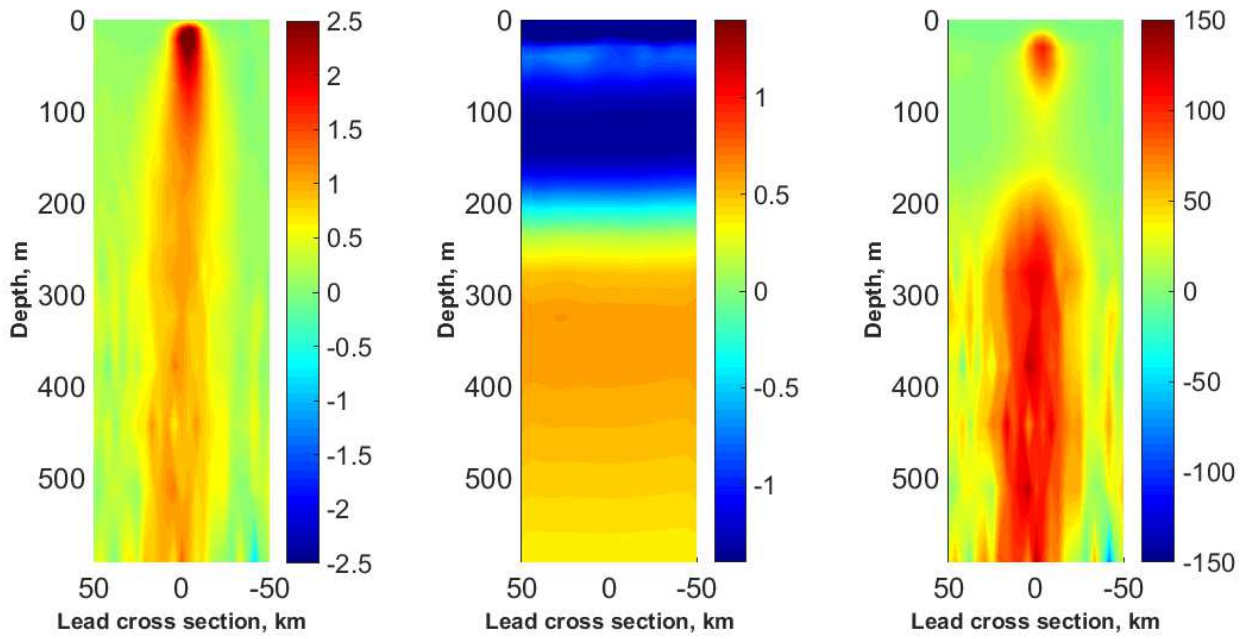


**Figure 10.** Vertical cross-section (thick black line in Figure 7) of (a) vertical velocity ( $\text{m}/\text{day}$ ), (b) temperature ( $^{\circ}\text{C}$ ), and (c) vertical ocean heat flux ( $\text{W}/\text{m}^2$ ), on the 7th January 2005.

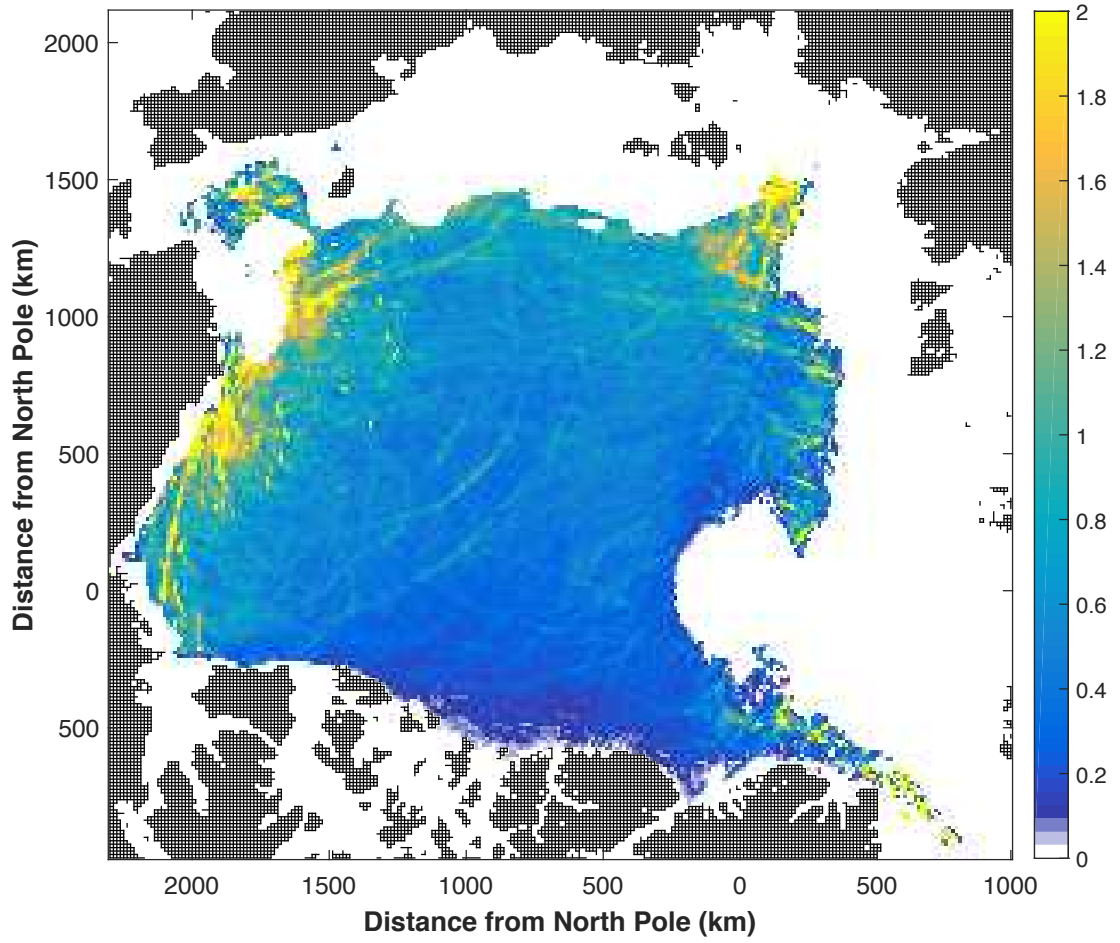


**Figure 11.** 1997-2008 winter mean vertical ocean heat flux ( $\text{W/m}^2$ ) derived from passive microwave sea-ice velocities and concentrations, and RGPS ice-velocity curl, assuming 1.5% lead fraction [Kwok, 2010] and using observed in-situ observations from *McPhee et al.* [2005] as anchor point. Maximum value of ocean heat flux along the alaskan coastline is  $17 \text{ W/m}^2$ . The colorbar is capped at  $2 \text{ W/m}^2$ .

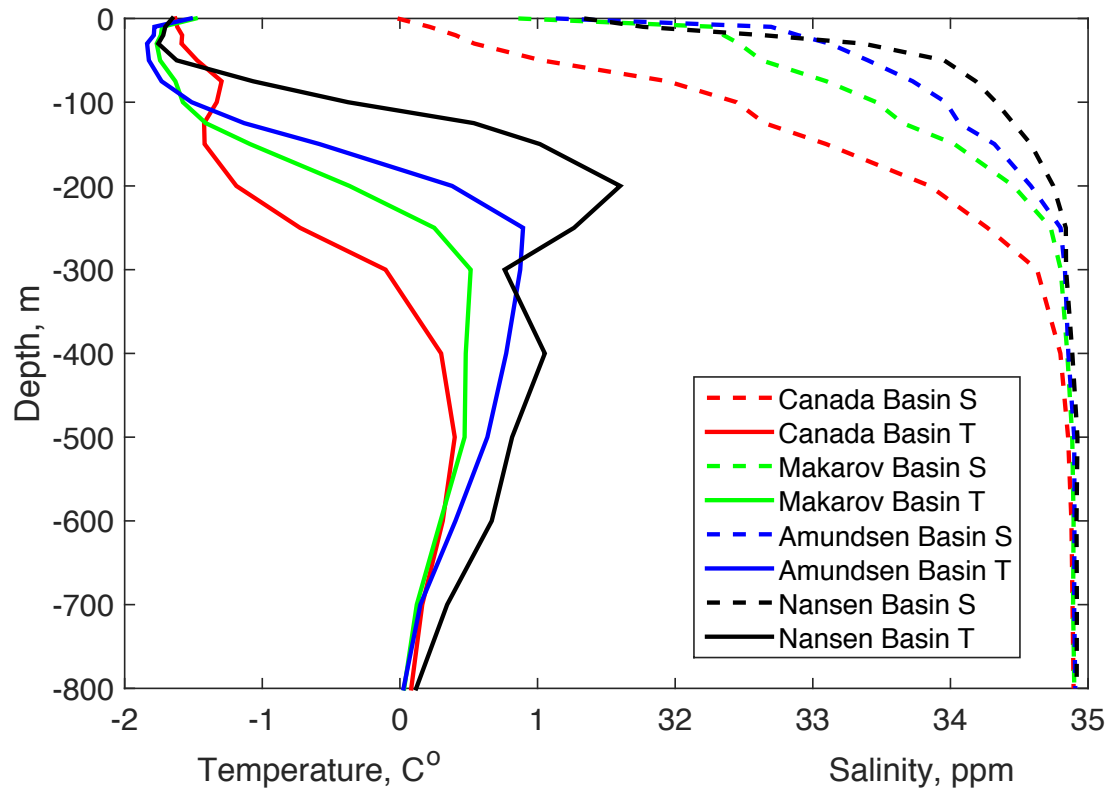


**Figure 12.** Mean Temperature and Salinity vertical profiles in the Canada, Makharov, Amundsen and Nansen Basins based on WOA2005 data. Note that the NSTM is only apparent in the Canada basin, but that heat is present beneath the mixed layer (in the halocline) in all Basins.



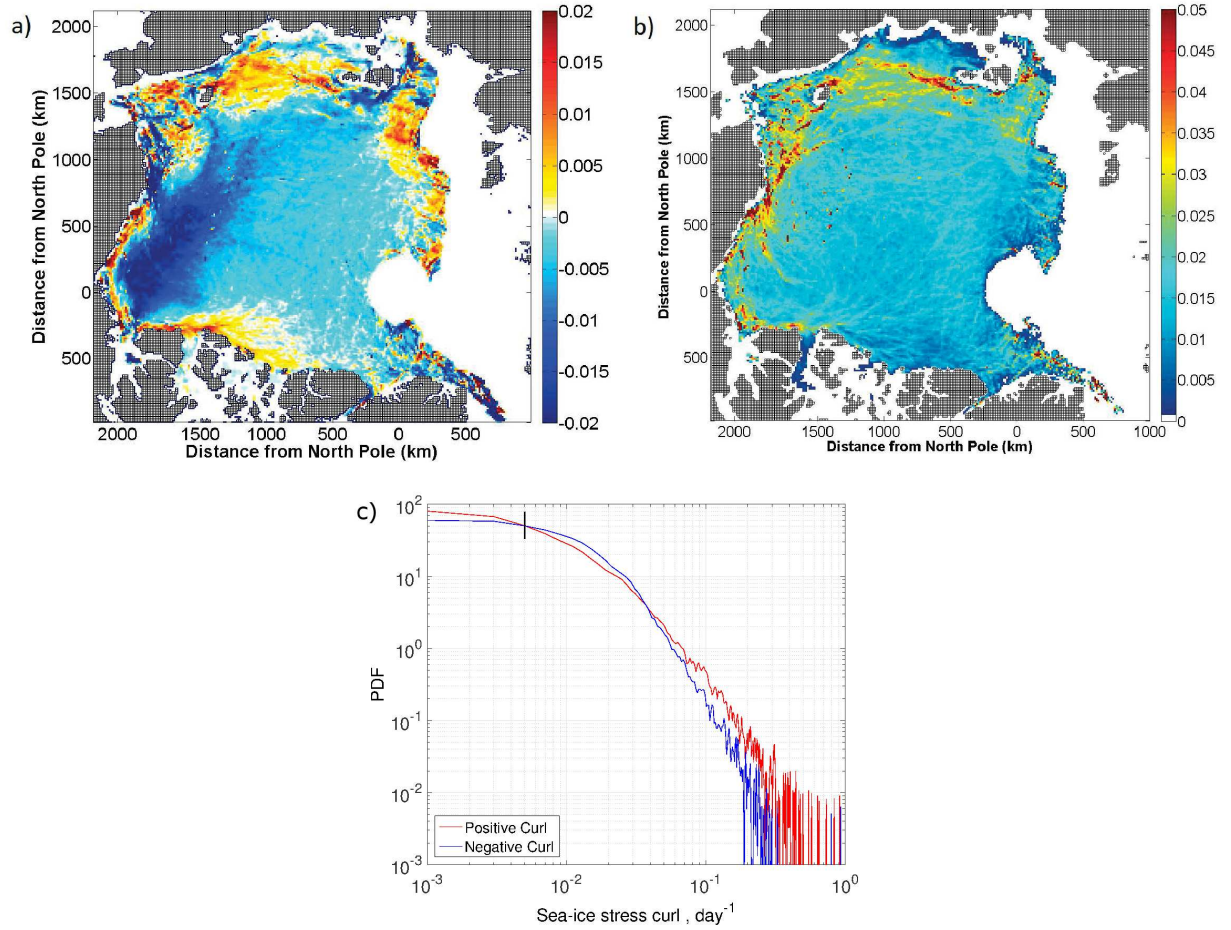


**Figure 13.** (a) 1997-2008 winters mean sea-ice velocity curl ( $\text{day}^{-1}$ ), (b) 1997-2008 winter mean sea-ice velocity curl ( $\text{day}^{-1}$ ) considering only positive values for RGPS data. Winter is defined as NDJFM and (c) PDF of sea-ice velocity curl for the Beaufort Sea region from the RGPS data. The mean curl over the 10-year simulation period is  $-0.007 \text{ day}^{-1}$ . Vertical bar in the figure represents the minimum curl that can be resolved based on the error in the drift estimates.